Impact of the 2016 Southeastern U.S. Wildfires on the Vertical Distribution of Ozone and Aerosol at Huntsville, Alabama

Bo Wang[1,2], Shi Kuang[3], Gabriele G. Pfister[4], Arastoo Pour-Biazar[3], Rebecca R. Buchholz[4], Andrew O. Langford[5], Michael J. Newchurch[2]

[1]Department of Earth and Environment, Boston University, Boston, MA, USA
[2]Department of Atmospheric and Earth Science, University of Alabama in Huntsville, Huntsville, AL, USA
[3]Earth System Science Center, University of Alabama in Huntsville, Huntsville, AL, USA
[4]Atmospheric Chemistry Observations and Modeling Laboratory, NCAR, Boulder, CO, USA
[5]Chemical Sciences Laboratory, NOAA Earth System Research Laboratories, Boulder, CO, USA

Key Points:

- Fires contribute 12–32 μg/m^3/hr (44–70%) to surface $PM_{2.5}$ and 7–8 ppb/10 hrs (30–37%) to daytime ozone at Huntsville.
- Fire-impacted ozone below 1 km is dominated by advection on 12 November and by local photochemistry on 13 November.
- Increasing aerosol fire emissions by a factor of 3–4 better matches observed AOD, $PM_{2.5}$ and DIAL aerosol extinction.

Corresponding author: Bo Wang, bowang@bu.edu

Abstract

We present an integrated analysis of measurements from ozonesonde, ozone (O_3) Differential Absorption Lidar (DIAL), ceilometer, surface monitors, and space-borne observations in conjunction with the regional chemical transport model Weather Research and Forecast Model with Chemistry (WRF-Chem) to investigate the effect of biomass burning emissions on the vertical distribution of ozone and aerosols during an episode of the 2016 Southeastern United States wildfires. The ceilometer and DIAL measurements capture the vertical extent of the smoke plumes affecting the surface and upper air over Huntsville, AL. The model evaluation results suggest a scaling factor of 3–4 for the wildfire aerosol emissions in order to better match observed aerosol optical depth (AOD), fine particulate matter ($PM_{2.5}$), and DIAL aerosol extinction. We use the scaled emissions together with WRF-Chem tendency diagnostics to quantify the fire impacts and characterize the processes affecting the vertical ozone budget downstream of the wildfires. During the daytime at Huntsville on 12 and 13 November, we estimate that fire emissions contribute 12–32 $\mu g/m^3$ (44–70%) to hourly surface $PM_{2.5}$ and 7–8 ppb/10 hrs (30–37%) to the surface ozone increase (ΔO_3), respectively. Net chemical ozone production (PO_3) is the main contributor to upper-air ozone, which reaches 17–19 ppb/10 hrs with an estimated 14–25% contribution from fire sources. Vertical mixing and advection are the major drivers of changes in surface ozone. Model analysis indicates that advection dominates ΔO_3 due to fire emissions below 1 km on 12 November, while local photochemistry dominates on 13 November. These results quantify the different mechanisms through which fires can influence the vertical ozone budget and point out uncertainties in fire inventories that need to be addressed in light of the increasing role of wildfires on air quality.

1 Introduction

Biomass burning (BB) releases substantial amounts of aerosol and ozone precursors that can affect climate and air quality (Crutzen et al., 1979; Crutzen & Andreae, 1990; Andreae & Merlet, 2001; Akagi et al., 2011). Previous observation and modeling studies have indicated that BB emissions contribute to local and regional air-quality problems (Hodzic et al., 2007; Pfister et al., 2008; Jaffe et al., 2013; Wigder et al., 2013; Baker et al., 2016), as well as to downwind pollution via long-range transport (McKeen et al., 2002; Colarco et al., 2004; Jaffe et al., 2004; Sapkota et al., 2005; Morris et al., 2006; Martin et al., 2006; Lapina et al., 2006; Cook et al., 2007; Oltmans et al., 2010; Lindaas et al., 2017; Rogers et al., 2020). These studies demonstrate that the impacts of biomass burning on air quality can vary dramatically over time and space. Models can be used to investigate the mechanisms through which BB influences air quality. However, more efforts are required to assess how current models capture the variability of BB impacts, especially at higher spatial and temporal resolution.

Chemical transport models (CTMs) have been widely used to estimate fire impacts. CTMs can provide good spatio-temporal coverage, differentiate the impacts of specific sources, and support mechanistic understanding of chemical and dynamical processes (Baker et al., 2018); however, amongst other issues, large uncertainties in fire-emission estimates present challenges for estimating the variability of fire impacts. These uncertainties can arise from limitations of satellite detection and inherent uncertainties of the empirical approaches used for emission estimations (Justice et al., 2002; van der Werf et al., 2017; Wang et al., 2018; Liu et al., 2020; Carter et al., 2020). The emission factors (EFs, the mass of a pollutant emitted per unit mass of biomass burned) are critical inputs for fire-emission models, but they vary by fuel type and fire conditions. While knowledge of EFs has increased substantially over the past decade, the uncertainty and natural variation in EFs remained a large source of uncertainties in BB emission estimates (Andreae & Merlet, 2001; Akagi et al., 2011). Furthermore, a large discrepancy of emission estimates

could exist between the bottom-up and top-down approaches. For instance, top-down constraints are applied on aerosol emissions to match smoke aerosol optical depth (Kaiser et al., 2012; Darmenov & da Silva, 2013). However, these global constraints are not applied in all fire inventories and may bias smoke estimates at regional to local scales. Recent studies show that temperate North America has much larger discrepancies in carbonaceous aerosols estimates than many other regions (Carter et al., 2020; Liu et al., 2020). These studies highlight the importance of further investigation and require observations at all scales (surface, aloft, and satellite).

Although satellites and surface monitors make routine measurements of atmospheric O_3 concentration, balloon soundings and lidar techniques can provide precise vertically resolved O_3 observations throughout the troposphere and lower stratosphere (Thompson et al., 2011). This vertical information significantly benefits air-quality management and modeling improvement (Cooper et al., 2015). We take advantage of both ozonesonde (Newchurch et al., 2003) and ozone lidar (Kuang et al., 2011) techniques at the University of Alabama in Huntsville (UAH) to measure the vertical distribution of key atmospheric parameters. The UAH ozone lidar is affiliated with the Tropospheric Ozone Lidar Network (TOLNet, https://www-air.larc.nasa.gov/missions/TOLNet/). Under a collaborative protocol, the TOLNet lidars have demonstrated their feasibility and capability in fire studies (Langford et al., 2015; M. Johnson et al., 2016; Kuang et al., 2017; Reid et al., 2017; Strawbridge et al., 2018; M. Johnson et al., 2021) and scientific projects (Leblanc et al., 2018; Sullivan et al., 2019; Gronoff et al., 2019). The continuous profiling of ozone and aerosols provides details missed by isolated measurements and is an asset for model evaluation by coordinating measurements (Langford et al., 2018, 2019). In addition, the ultraviolet (UV) backscatter (or extinction) profiles retrieved from ozone lidar can quantify the aerosol variability at high spatio-temporal resolution, and these measurements serve as a tracer for fire smoke (Kuang et al., 2020; Langford et al., 2020). To our best knowledge, there has been little or no attempt to evaluate CTMs using this range-resolved UV aerosol optical product.

Coordinating vertical observations and simulations can also improve our understanding of the fire impacts on vertical profiles. Due to multiple O_3 sources in the troposphere and a lack of coincident measurements at sufficient spatial resolution, combining observations and modeling is crucial for understanding the O_3 production from fire emissions (Fiore et al., 2014). The diagnostics of trace-gas tendencies in CTMs output are widely used to identify the drivers for ozone production due to varied anthropogenic and natural sources (Barth et al., 2012; Lu et al., 2018; Hu et al., 2019; Pfister et al., 2019), while fewer studies for biomass burning sources have been completed. In this study, the O_3-tendency diagnostics, together with sensitivity simulations both with and without fire emissions, allow exploration of the roles of chemical and dynamical processes affecting the vertical O_3 accumulation downstream of fires. The enhancement of the local vertical O_3 distribution due to fire emissions is expected to arise from multiple processes, including local photochemistry (e.g., photochemical reaction of the O_3 precursors from fire emissions), transport of ozone by upwind smoke plumes, and the vertical exchange (e.g., redistribution of O_3 by interactions between surface and upper air). In this study, we coordinate a range of different data sets and methods to understand the impact of these different processes on the vertical O_3 variability in fire smoke.

With a relatively flat topography in the Southeastern United States (SEUS) region, the region around Huntsville, AL was usually dominated by local anthropogenic, biogenic, and agricultural burning emissions at the surface, while wildfire plumes typically prevail in the free troposphere (FT) (Reid et al., 2017). Our case study of an episode when Huntsville was affected by the 2016 SEUS wildfires shows that smoke can affect ozone and aerosol loadings at the station both at the surface and in the upper air. Using comprehensive observations (Huntsville ground-based lidars, in-situ measurements, spaceborne observations) to evaluate the performance of regional model simulations results

in a framework to estimate the vertical variability of these fire impacts. Coordinating vertical observations and modeling provides additional value in assessing model performance and enhances the scientific understanding. The following objectives comprise this study: (1) Evaluate the model performance against regional and local observations, especially vertical ozone and UV aerosol extinction profiles, to understand the model capabilities and limitations in reproducing the observations. (2) Characterize the chemical and dynamical processes affecting the vertical ozone accumulation in smoke plumes and understand the roles of local chemical reactions, transportation, and vertical exchange. (3) Vertically quantify the contribution from fire emissions to net chemical ozone production and particulate matter.

2 Data and Methods

2.1 Wildfires Episode and Study Area

The 2016 Southeastern United States (SEUS) wildfires series occurred along the Southern Appalachians throughout October and November 2016 and burned over 158,000 acres across six Southern states (see Table S1 in the supporting information). Multiple factors contributed to the extraordinary wildfire outbreak and spread, including an exceptional drought, deep leaf litter and duff layers, many human ignitions with relatively few lightning strikes, episodic strong winds by frontal systems, and complex mountain landscapes (Konrad & Knox, 2017; Williams et al., 2017). We focus on a high-pollution episode when smoke influenced the Huntsville station and the SEUS region during 12–14 November 2016. Figure 1a shows the locations and names of the 14 largest active wildfires during this study period. Figure 1b shows the study domain with surface $PM_{2.5}$ and O_3 monitoring sites indicated. The Huntsville station is located in North Alabama on the UAH campus.

2.2 Huntsville Station Facilities

Both the ceilometer and the ground-based O_3 DIfferential Absorption Lidar at the UAH campus (34.725° N, 86.645° W) detect the vertical aerosol structure. Balloon-borne Electrochemical Concentration Cell (ECC) ozonesondes launched from the UAH campus allow the measurement of the vertical O_3 concentration in smoke plumes. Both DIAL (aerosol extinction and O_3) and ozonesonde data are used to assess how well the model captures the vertical distribution of O_3 and aerosol loadings.

Although primarily designed to detect cloud heights, ceilometers have the capability for a quantitative retrieval of the aerosol backscatter coefficient (Wiegner et al., 2014). The Vaisala CL51 ceilometer used in this study is a pulsed diode-laser lidar (905 nm) in the UAH Mobile Integrated Profiling System (MIPS) (Wingo & Knupp, 2015). The ceilometer, located on the UAH campus, measures backscatter profiles up to 15 km above ground level (AGL) with high spatial and temporal resolution at 30 m and 15 s, respectively. Because the backscatter signal is dominated by the aerosol component at 905 nm, the total backscatter intensity serves as an indicator of relative aerosol loading during 12–14 November 2016.

The UAH campus also houses one of the TOLNet O_3 DIAL systems, named the Rocket-city O_3 Quality Evaluation in the Troposphere (RO_3QET) lidar. RO_3QET measures vertical O_3 profiles from 0.1 km up to 10 km above the ground using 289 and 299-nm lasers with an uncertainty of about ±10% (Kuang et al., 2011). The temporal resolution of the lidar sampling is adjustable and is typically set at 10 minutes. The vertical resolution varies with altitude to obtain sufficient lidar signal-to-noise ratio and is between 150 and 300 m in the planetary boundary layer (PBL). Aerosol extinction coefficients at the non-absorption line (299 nm) are retrieved by assuming a constant aerosol extinction-to-backscatter ratio, which is 60 steradians (sr) for this study. Validation ex-

periments through comparing with co-located high spectral resolution lidar (HSRL) observations suggest that the RO_3QET lidar is capable of capturing aerosol variability up to 6 km altitude at high spatio-temporal resolution (Kuang et al., 2020).

The Huntsville ECC ozonesonde attached with a radiosonde provides vertical profiles of ozone, temperature, relative humidity (RH), and wind. In this study, the data are derived from one of the weekly flights at the Huntsville ozonesonde station, which makes observations from the surface up to 35 km with a vertical resolution of 100 m (Newchurch et al., 2003). The ozone measurements have a precision better than ±5% and an accuracy better than ±10% (B. Johnson et al., 2002).

2.3 Surface Data and Satellite Products

Hourly $PM_{2.5}$ and O_3 measurements retrieved from the Environmental Protection Agency (EPA) (https://www.epa.gov/outdoor-air-quality-data) are used to evaluate the model performance for the surface air quality within the smoke-impacted region. Moderate Resolution Imaging Spectroradiometer (MODIS) Collection 6 Level 2 10 km merged Dark Target/Deep Blue aerosol optical depth data onboard Terra and Aqua (MOD04_L2 and MYD04_L2) (Levy et al., 2015) acquired from the NASA Earth Data Level-1 and Atmospheric Archive & Distribution System Distributed Active Archive Center (LAADS DAAC) website (https://ladsweb.modaps.eosdis.nasa.gov/) is used to evaluate the model performance for the horizontal plume extent. To compare MODIS AOD at 10-km resolution with WRF-Chem AOD at 4-km resolution, we regrid both MODIS and modeled AOD to a $0.1^\circ \times 0.1^\circ$ grid. For each grid box, MODIS AOD at 550 nm is calculated as the mean of Aqua AOD at 19 UTC and Terra AOD at 17 UTC (or 16 UTC on 13 November), WRF-Chem AOD at 550 nm is calculated as the mean of modeled AOD at 19 UTC and modeled AOD at 17 UTC (or 16 UTC on 13 November). Because WRF-Chem can directly output the variable "EXTCOF55", which represents layer aerosol extinction coefficients for 550 nm, we define modeled AOD at 550 nm as the vertical sum of each the "EXTCOF55" field multiplied by the layer depth. Visual images from MODIS and the Visible Infrared Imaging Radiometer Suite (VIIRS), available via the NASA Worldview website (https://worldview.earthdata.nasa.gov/), are used to qualitatively assess smoke plume coverage and fire detection from thermal anomalies. The sensor resolutions of MODIS and VIIRS hotspot detections are 1 km and 375 m, respectively.

2.4 Model Description and Experiment Design

A fully coupled meteorology-chemistry model, the Weather Research and Forecasting with Chemistry model WRF-Chem (Grell et al., 2005; Fast et al., 2006) version 3.9.1 is applied in this study. The model configurations are listed in Table 1. For this study we selected the Model for Ozone and Related chemical Tracers (MOZART) gas phase chemical scheme (Emmons et al., 2010) coupled with the Georgia Institute of Technology–Goddard Global Ozone Chemistry Aerosol Radiation and Transport (GOCART) aerosol scheme (Chin et al., 2000), referred to as MOZCART (Pfister et al., 2011). Other parameterizations include the Morrison's microphysics scheme, the Rapid Radiative Transfer Model (RRTM) longwave and Goddard shortwave radiation schemes, the Monin-Obukhov surface layer, the Noah Land Surface Model, the Yonsei University (YSU) PBL, the New Grell cumulus scheme (G3), and the simplified Tropospheric Ultraviolet-Visible photolysis scheme (F-TUV). National Centers for Environmental Prediction (NCEP) North American Mesoscale (NAM) 12 km Analysis data (https://rda.ucar.edu/datasets/ds609.0/, accessed 7 February 2018) provide initial and lateral boundary meteorological conditions. MOZART-4 global model outputs provide the initial and lateral chemical conditions. Biomass burning emissions are calculated using the Fire Inventory from NCAR (FINNv1.5) (Wiedinmyer et al., 2011) and the online plume-rise model (Freitas et al., 2007). FINNv1.5 is based on fire counts derived from the Moderate Resolution Imaging Spectroradiometer (MODIS). The hourly emissions are allocated using the standard WRAP diurnal profile (WRAP,

2005). For the MOZCART scheme, the aerosol emissions are speciated from FINNv1.5 particulate matter (PM). The speciation as provided in the emission preprocessor is listed in Table S2. Anthropogenic emissions for both area and point sources are obtained from the 2011 U.S. EPA national emissions inventory (NEI 2011 v2). Biogenic emissions are calculated online using the Model of Emissions of Gases and Aerosols from Nature (MEGAN) module (Guenther et al., 2006).

Two nested domains cover CONUS and SEUS with 16 km and 4 km horizontal resolutions, respectively. The vertical coordinate comprises 60 unequally spaced layers below 50 hPa, with 12 layers below 2 km altitude and a center height of 28 m for the lowest layer (see vertical grids structure in Figure S1). The simulation time period ranges from 8 to 14 November 2016 with the first four days used as model spinup. To ensure that the model represents accurate meteorology, we use nudged meteorological fields and in addition conduct a meteorology reinitialization every 24-hour, but recycle the initial chemical fields from the end of the previous day. The evaluation of the surface temperature is shown in Figure S11 and demonstrates the continuity of simulated meteorological fields despite the 24-hour reinitialization. Three simulations are performed to estimate the wildfire impacts (Table 1): the CTRL simulation contains no fire emissions; the FIREorig simulation contains the original fire emissions (speciated from FINNv1.5 $PM_{2.5}$ and PM_{10}) without emissions correction; the FIREcorr simulation contains the fire emissions with emissions adjustment (description in Section 3.2). In order to generate identical meteorology for the sensitivity analysis on fire-impacted O_3, the aerosol-radiation feedback is disabled.

2.5 Fire Inventories and Burn Area Products

The Monitoring Trends in the Burned Severity database (MTBS; https://www.mtbs.gov) provides information on the total number of acres burned since ignition and is used to indicate large wildfires (Table S1). To investigate the emission inputs, we estimate the daily burn area for each wildfire (Figure 2) by aggregating the FINNv1.5 burn area in the geospatial bounding box from the MTBS wildfire database. The fire emission inputs for this work (FIREorig and FIREcorr simulations) are compared with four MODIS-based fire inventories: FINNv1.5, the Global Fire Emissions Database (GFEDv4s) (van der Werf et al., 2017), the Global Fire Assimilation System version 1.2 (GFASv1.2) (Kaiser et al., 2012), and the Quick Fire Emissions Database version 2.5_r1 (QFEDv2.5_r1) (Darmenov & da Silva, 2013).

3 Results

3.1 Horizontal and Vertical Plume Transport

In this section, we discuss the horizontal and vertical plume transport using satellite and ground-based lidars and identify the smoke-impacted period, which is used later for model evaluation and diagnostic analysis. Our analysis reveals that the daily and diurnal variations of smoke transport are mediated by synoptic weather conditions and the PBL evolution.

In Figure 3, MODIS AOD and MODIS imagery show that the wildfires along the Southern Appalachians continued to burn and emitted a significant amount of smoke over the SEUS region during 12–14 November 2016. This time period is chosen for later model evaluation and analysis. NOAA WPC surface analysis (Figure S2) shows that a cold front passed over the wildfire region during 12-18 LT on 11 November. After the frontal passage, smoke stretched across portions of the SEUS region driven by northeasterly winds on 12 November. As a high-pressure circulation dominated the following two days, AOD shows less spreading pattern, with a more concentrated distribution around the location of the wildfires.

The UAH ceilometer captured the aerosol plumes downwind of the fires, as shown in Figure 4. The time-height curtain of backscatter intensity shows that several plumes passed over Huntsville in the nighttime residual layer (RL) (Figure 4a). Some plumes subsided toward the surface before sunrise; others were entrained by a developing PBL in the morning and then mixed vertically throughout the PBL. This mixing provides a mechanism for fire emissions to contribute to the downwind air quality over night. In addition, an elevated aerosol plume stayed at ∼2 km AGL from 12 UTC (6 LT) on 12 November to 12 UTC (6 LT) on 13 November. This plume is likely fire smoke as MODIS shows obvious smoke spreading over Huntsville (Figure 3).

The most severe surface particulate air pollution at Huntsville occurred on 13 November, when an air-quality alert was issued for Madison and Morgan counties in the afternoon instigating DIAL measurement from 19:37 to 22:17 LT on 13 November under this high aerosol loading condition. The time-height curtain of the aerosol extinction coefficient at 299 nm (Figure 4b) shows heavy background aerosols and relatively dense plumes within that domain. The background aerosols below the capping inversion layer (∼0.5/km below 1.5 km AGL) results from sufficient daytime mixing in the well-developed PBL. A relatively dense plume (>1.0/km) features about four times higher extinction (>1.0/km) compared to typical aerosol loading conditions. At 22 LT, the dense plume extended across the whole RL column and evolved to be a thicker layer (∼0.7 km thickness) between two finer layers. The specified fine structure is highly consistent with the ceilometer backscatter observation (Figure 4c). Ozonesonde and DIAL measurements are used to assess the model performance on 12 and 13 November, respectively.

3.2 Model Performance for AOD and Emissions Adjustment

In this section, the modeled spatial pattern of smoke plumes is assessed against satellite observations. Results uncover limitations that lead to an adjustment of the emission inputs, which is further justified by comparing our emission inputs with four fire inventories.

Comparing WRF-Chem AOD to MODIS AOD for 12–14 November (Figure 3 and Figure S3) suggests that the simulation "FIREorig" is able to reproduce the overall spatial pattern of smoke plumes over the SEUS, with a spatial correlation coefficient between modeled and observed AOD of 0.6 on average (0.4 on 12 November, 0.7 on 13 and 14 November). The lower correlation on 12 November is associated with the prediction bias of the frontal passage during 00–18 UTC on 12 November, indicated by the front locations in surface analysis and modeled result (Figure S2). Despite the general agreement in AOD distribution, there is an underestimation of the model in the AOD magnitude. We calculate an averaged scaling ratio r by averaging the three different slopes for 12–14 November (MODIS AOD/FIREorig Modeled AOD = 3.6). Thus, the domain-averaged observed AOD is about 3.6 times the simulated AOD. The reasons for this could be uncertainties in emission estimations (Zhang et al., 2014; Pereira et al., 2016), inadequate assumptions of aerosol optical properties (Curci et al., 2015), the use of simplified aerosol chemistry modules without representation of secondary organic aerosol (Fast et al., 2006), or misrepresentation of transport processes (Aouizerats et al., 2015; Wu et al., 2017). Quantifying each bias is a challenge beyond our scope. In this case study, we focus on exploring the uncertainties of emissions only and increase the original fire aerosol emissions by a factor of 3.6, without changing the fire gas-phase emissions. Specifically, we multiply all aerosol components (unspeciated $PM_{2.5}$, PM_{10}, organic carbon, black carbon, and sulfate) in the original gridded fire emissions by 3.6. This adjustment improves the model performance of the domain-averaged AOD and changes the average slope from 3.6 (MODIS Vs. FIREorig Modeled AOD) to 1.1 (MODIS Vs. FIREcorr Modeled AOD), as shown in Figure S3. Although this approach does not rectify all the uncertainties in the emission estimates and may not reflect the temporal-spatial variations of smoke behavior, our

sensitivity study can help constrain the emission estimates based on satellite observations.

To justify the scaling of the fire aerosol emissions, we compare emissions from the original simulation (FIREorig) and the simulation with scaled aerosol emissions (FIREcorr) to the inter-inventory differences. Figure 5 shows the ratio of carbonaceous aerosols (both organic carbon OC and black carbon BC) to carbon monoxide CO in different fire inventories and our simulations. Each data point indicates daily fire emission summed over the wildfire region of interest defined in 33.46–38.17° N and 78.75–86.25° W (see the selected region in Figure S4). The four inventories show considerable discrepancies in the emissions ratios for November 2016 over the wildfire area. The (OC+BC)/CO ratio is about 0.07, 0.09, 0.11 and 0.4 in Gg/Gg for FINNv1.5, GFASv1.2, GFEDv4s and QFEDv2.5_r1, respectively. Such a broad range of emission ratios justifies our choice to scale the emission input from 0.08 Gg/Gg to 0.3 Gg/Gg.

Emission differences may arise from inventory-specific methods for estimating the amount of burned vegetation, the vegetation type, and the emission factors. Although all of the four inventories are based on MODIS fire detections, FINNv1.5 converts the MODIS active fire product into burned area generally by assuming an upper limit of area burned and further scaling it by the percent of bare cover (Wiedinmyer et al., 2011); GFEDv4s primarily uses the MODIS burn area product retrieved from pre-burn and post-burn images and ingests active fire locations for its small fire boost (Randerson et al., 2012; Giglio et al., 2013; van der Werf et al., 2017); GFASv1.5 assimilates MODIS Fire Radiative Power (FRP) (Kaiser et al., 2012); QFEDv2.5_r1 uses MODIS FRP directly combined with a scaling factor derived by a top-down constraint for different biomes (Darmenov & da Silva, 2013). All four inventories also differ in the vegetation types used, and while they generally use emission factors from Andreae and Merlet (2001) and Akagi et al. (2011), they use different updates and also aggregate these emission factors differently. Consequently, the (OC+BC)/CO ratios over the SEUS wildfire region differ by a factor of 5.7 (Figure 5). Our analysis is consistent with previous assessment about the uncertainties in fire aerosol emissions. Carter et al. (2020) showed that fire aerosol emissions from different inventories differ by a factor of 4 to 7 over North America. Liu et al. (2020) showed that temperate North America has a coefficient of variation as high as 102% for mean annual OC+BC emissions among fire inventories. Our choice of a scaling factor of 3.6 sets our emissions within this discrepancy envelope. The scaling of fire aerosol emissions is also supported by previous studies (Wiedinmyer et al., 2011; Kaiser et al., 2012; Darmenov & da Silva, 2013), which addressed the need for observation constraints on the bottom-up estimates of fire aerosol emissions, especially for a given fire event.

3.3 Model Performance for Surface $PM_{2.5}$ and Vertical Extinction

Using the adjusted emission inventory, we assess how well the model simulates surface $PM_{2.5}$ and the vertical aerosol loading by comparing the model results with observations from surface monitors, lidar, and satellite.

Figure 6 shows the time series of U.S. EPA $PM_{2.5}$ observed and modeled $PM_{2.5}$ from three sensitivity simulations. The FIREorig simulation shows an obvious underestimation of observed $PM_{2.5}$ with a domain-wide mean bias of -21.6 $\mu g/m^3$ against hourly observations from all 8 sites. The standard deviations normalized with respect to observations are much lower than 1.0 (see pattern statistics in Figure S5), with a domain-averaged value of 0.3 among all 8 sites. After the emission adjustment, the FIREcorr simulation is able to capture the domain-averaged magnitude (as the mean bias reaches -0.4 $\mu g/m^3$ and the normalized standard deviation reaches 1.0) and reproduce the maximum hourly $PM_{2.5}$ ($\sim$200 $\mu g/m^3$ on 12 November at Site 1). Additionally, the FIREcorr simulation reveals dominant fire contributions to the observed $PM_{2.5}$ exceedance of the air qual-

ity standard (35 μg/m^3 for 24-hour limit), especially at the rural sites nearby the wildfires.

Despite the improvement in magnitude, the domain-averaged correlation coefficient just slightly increases from 0.5 to 0.6, as a domain-averaged scaling factor cannot improve the model performance for the diurnal variations. Both FIREorig and FIREcorr simulations perform well in reproducing the diurnal cycle at Sites 3–7 but perform poorly at Sites 1, 2, and 8. Statistically, modeled and observed $PM_{2.5}$ have a strong to moderate correlation at Sites 3–7 and weak correlation at Sites 1, 2, and 8. This model bias in the diurnal fire behavior can be partly explained by satellites providing information at the overpass time only (Wang et al., 2006), biases in wind field, and the domain-averaged scaling factor adopted here. Other potential error sources are discussed later.

Figure 7 shows the comparison between the DIAL-retrieved aerosol extinction (at 299 nm) and the simulated vertical aerosol extinction (at 300 nm) for 19–23 LT on 13 November. The FIREcorr simulation is able to capture the nocturnal boundary layer aerosol extinction ($\sim$0.5/km below 1.5 km AGL), while the FIREorig simulation underestimated the magnitude. This comparison indicates that the improved simulation can reproduce the well-mixed smoke during the daytime PBL development. However, the FIREcorr simulation misses the densest plume (>1.0/km after 20 LT on 13 November) observed by DIAL, underestimates the highest MODIS AOD nearby wildfires (observed at noon on 13 November in Figure 3) and underestimates $PM_{2.5}$ at one site nearby the wildfire (e.g., Site 2). A likely reason for the underestimate is missing fire sources.

To confirm this hypothesis, we examine both MODIS and NPP/VIIRS reflectance images with the fires and thermal anomalies product (Figure S9), compared to the FINNv1.5 daily burn area grouped by each wildfire (Figure 2). It was cloudy and hazy over the wildfires region on 13 November, conditions that obscure satellite detection. Although some wildfires emitted visible dense smoke plumes (e.g., the Rough Bridge Fire in north Georgia) and were counted in the NPP/VIIRS night detection, the fires were not counted by the MODIS thermal anomalies product. Consequently, the burn areas for many wildfires are zero on 13 November in the FINNv1.5 inventory. Two other MODIS-based inventories (GFASv1.2 and QFEDv2.5_r1) also report small aerosol and gas emissions on 13 November (Figure S7). These differences imply that the clouds and thick haze probably obscured the MODIS fire detection on 13 November. The detection limitation is likely associated with attenuated fire signal and solar heating during the day and the potential cloud/smoke classification issues (Justice et al., 2002; Polivka et al., 2016). As a result, the model using the MODIS-based fire inventories could not reproduce some freshly-emitted smoke plumes.

3.4 Model Performance for Surface Ozone and Vertical Ozone

This section reports the comparison of modeled O_3 with surface monitors, ozonesonde, and DIAL measurements. Because aerosol-radiation feedback has been turned off in the simulations to generate identical meteorology, and heterogenous or aqueous chemistry is not considered in the MOZCART mechanism, the modeled O_3 is identical in the FIREorig and FIREcorr simulations.

Figure 8 shows the time series of observed and modeled O_3 in sensitivity simulations. The model generally reproduces the observed surface O_3 level (below 60 ppb) during 12–14 November at most sites with a domain-wide mean bias of +4.7 ppb against hourly observations from all 6 sites. The results show consistent diurnal variations between simulated and observed O_3 at both rural and urban sites, with strong to moderate correlation coefficients (see pattern statistics in Figure S6). Among all the sites, the normalized standard deviation and correlation coefficient of domain-averaged O_3 are 1.0 and 0.6, respectively. As for individual sites, the model performance at Sites 3 and 5 is weaker, indicated by a low correlation coefficient and high normalized root-mean-square

(NRMS) error. Interpreting uncertainties in modeled O_3 is complicated because of impacts from meteorology, emissions, and model parameterizations. The uncertainty in fire emissions is only one of many possible sources for the uncertainties in modeled O_3. Other factors, such as the transport bias during the frontal passage, the model's capability in reproducing the nocturnal stable layer, and the accuracy of anthropogenic and biogenic gaseous emissions, might induce larger model uncertainties. The difference between FIREcorr and CTRL simulations suggests that the total fire impact on surface O_3 concentration was less than 10 ppb at most sites.

An ozonesonde was launched from the UAH campus at 13 LT on 12 November. Figure 9 compares modeled results with the observed vertical profiles, including ozone volume mixing ratio, relative humidity, potential temperature (θ), horizontal wind speed, and horizontal wind direction. The ozonesonde reveals an enhanced O_3 lamina between two θ inversion layers between 1.4–2.3 km. It peaks at 1.8 km AGL with 56 ppb, ∼12 ppb larger than concentrations in the PBL. This thick lamina co-existed with the elevated aerosol plume observed in ceilometer under a light northeasterly wind. The coexistence of a fire-impacted aerosol plume and enhanced O_3 suggests that wildfires contributed to the ozone lamina above the PBL. The difference between the CTRL and FIREcorr simulations indicates a slight ozone enhancement due to fire emissions at 13 LT over Huntsville, which is further analyzed at a regional scale in Section 3.5.1. Overall, WRF-Chem is able to reproduce vertical ozone and meteorological profiles in smoke plumes below 3 km. In particular, the model reproduces the wet and ozone-rich lamina, and simulates temperature and wind field consistent with observations; however, it is limited in simulating the finer inversion layers. The model predicts a slightly lower PBL height (1.2 km compared to 1.4 km), and it does not resolve the upper θ inversion at 2.3 km well. This limitation is likely due to the relatively coarse vertical resolution at ∼2 km and the bias in predicting wind shear when the wind turned sharply above the lamina, as observed by sonde. The underestimat in O_3 in the PBL is consistent with an underestimat in surface O_3 at the nearby site. This underestimate can be due partly to the model bias in wind direction and relative humidity in the PBL, as well as other factors discussed earlier. The model also reproduces the O_3 laminae observed by DIAL during 19–23 LT on 13 November (Figure 7), but it underestimates the O_3 magnitude in the nocturnal boundary layer, which underestimate might be caused by the uncertainties in emission inputs as discussed in the previous section.

3.5 Diagnosing Fire Impacts on Vertical O_3 and $PM_{2.5}$ Distribution

Because the model performs well in simulating the vertical and surface ozone distributions and reproduces the well-mixed aerosol during the daytime, we use the model to further analyze the vertical ozone accumulation in fire smoke during the daytime on 12 and 13 November 2016. We begin with a regional sensitivity analysis to show the overall fire impacts and the possible smoke sources, and then apply the model's tendency diagnostics to examine the processes contributing to the ozone accumulation over Huntsville.

3.5.1 Regional Sensitivity Analysis of Vertical Fire Impacts and Possible Smoke Sources

Figure 10 shows the modeled longitude-altitude curtain plots of O_3, fire-impacted O_3, and fire-impacted $PM_{2.5}$ at 13 LT (19 UTC) on 12 and 13 November over the SEUS region. On 12 November, the curtain (Figure 10a) shows that an enhanced O_3 lamina at 2 km ASL spreads widely from 78° W to 88° W and passes over the Huntsville station. This thick layer is spreading above the PBL and is capped below 3 km by a strong wind shear when the wind turns strongly westerly above ∼ 3 km. Figure 10b and 10c show the modeled fire impacts (FIREcorr minus CTRL) on O_3 and $PM_{2.5}$, respectively. The simulations show enhanced O_3 concentrations within the elevated smoke plume, consistent with our observation analysis. Quantitatively, the fires result in an O_3 enhance-

ment range of 2–5 ppb and a $PM_{2.5}$ enhancement range of 10–20 $\mu g/m^3$ at 13 LT along the west to east cross section. At 85–86° W, the enhancements estimated in O_3 and $PM_{2.5}$ can exceed 5 ppb and 20 $\mu g/m^3$, respectively. Using the modeled hourly $PM_{2.5}$ and AOD (not shown here), we estimate that the smoke plume is transported to Huntsville from multiple wildfires that occurred during the frontal passage on 11 November (see the large active wildfires in Figure 2 and wildfire map in Figure 1a). The wind-shear structure caps the mixed smoke plume with enhanced O_3 in the lowest level of FT. Below the elevated plume, there is slightly lower PBL O_3 enhancement (1–2 ppb) and $PM_{2.5}$ enhancement (5–15 $\mu g/m^3$) at 86–88° W. The smoke in the PBL is relatively fresh with < 6 hrs transport time and is likely emitted from nearby small fires on 12 November.

As the weather conditions turn to a high-pressure circulation on 13 November, a new pattern emerges with concentrated fire impacts from the surface up to 2 km ASL on a regional scale (Figure 10d–f). PBL O_3 increases in the stagnant air (Figure 10d), and the contribution of fires to O_3 and $PM_{2.5}$ increases (Figure 10e and 10f). Quantitatively, the fires result in a dominant O_3 enhancement range of 4–10 ppb or higher and a $PM_{2.5}$ enhancement range of 40–80 $\mu g/m^3$ or higher at 13 LT along the west to east cross section. A large portion of the well-mixed PBL smoke is emitted on 12 November, when the wildfires were most active during our study period (Figure 2). As illustrated in the observation analysis, the smoke remains in the residual layer overnight and can effectively be transported to affect other locations on the next day.

3.5.2 Local Process Analysis of Daytime-integrated and Diurnal Vertical Ozone Budget in Fire Smoke

Our sensitivity simulations confirm that fire emissions impacted the vertical ozone contribution over Huntsville on 12 and 13 November. This local enhancement could be caused by the transport of fire-related ozone and/or ozone precursors which increased local ozone production. The modeled results in Section 3.4 also imply that fires were not the only source contributing to the observed ozone laminae. This result brings up two questions: (1) What are the relative roles of chemical and dynamical processes on the vertical ozone accumulation? (2) What is the relative contribution of fire emissions to the total net photochemical ozone production? To address these questions, we analyze the processes affecting the vertical ozone distribution using the WRF-Chem tendency diagnostics, including net chemical ozone production PO_3 (Chem), horizontal and vertical advection of ozone (AdvH+AdvZ), vertical mixing of ozone (Vmix), and the sum of all process tendencies (SumTend). The daytime ozone tendency output from the sensitivity simulations with fire emissions (FIREcorr) and without fire emissions (CTRL) is used to explore the fire contribution. The following model results are averaged over 5×5 horizontal grids (20 km×20 km) over Huntsville for better representativeness.

Figure 11a and 11b show daytime-integrated (7–17 LT) O_3 process tendencies and $PM_{2.5}$ concentrations over Huntsville for the FIREcorr and CTRL simulations on 12 and 13 November, respectively. Here the FIREcorr and CTRL SumTend indicate the daytime-integrated change of ozone concentration (ΔO_3) in simulations with and without fire emissions, respectively. The absolute O_3 process tendencies show similar patterns on both days. In the upper air (0.2–2.0 km AGL), the positive PO_3 dominates the daytime ozone accumulation on both days. The total PO_3 peaks by 17 ppb/10 hrs at 1.6 km on 12 November and by 19 ppb/10 hrs at 0.5 km on 13 November. In the surface layer below 0.2 km, pronounced negative PO_3 is caused by the quick NOx titration near the surface (modeled NOx ∼15 ppb). However, ΔO_3 peaks near the surface by 18 ppb/10 hrs on 12 November and by 25 ppb/10 hrs on 13 November. The negative PO_3 near the surface is offset by positive O_3 contributions from vertical mixing and advection processes. Vertical mixing contributes positively near the surface yet negatively in the upper air, because it tends to disperse the enhanced O_3 from the upper air to the surface (Hu et al., 2019). The results imply that local chemical processes dominate the upper air ozone accumu-

lation while dynamical processes directly contribute to the ground-level ozone build-up over Huntsville.

Figure 11c and 11d extract the relative O_3 tendencies and $PM_{2.5}$ concentrations attributable to fires (FIREcorr minus CTRL) for 12 and 13 November, respectively. Here FIREcorr-CTRL SumTend indicates the daytime-integrated ΔO_3 due to fire emissions (Figure S8). During 12–13 November, fire emissions increase the vertical O_3 concentrations by affecting local chemical reactions, transportation, and the vertical airmass exchange. The daytime ΔO_3 due to fire emissions is similar on both days, which peaks near the surface at 7 ppb/10 hrs on 12 November and at 8 ppb/10 hrs on 13 November. However, the dominant processes contributing to the total signals show daily and vertical variability. On 12 November, an increase of positive PO_3 dominates the upper-level (above 1.2 km) fire-impacted O_3 accumulation, while the transport process dominates at the lower level. In contrast, on 13 November, an increase in PO_3 (either through increased ozone chemical production or a decrease in ozone chemical loss) dominates the lower level (below 1.0 km), while transport processes dominate at the upper level. The decrease of negative PO_3 in the surface layer (i.e., PO_3 is more negative in CTRL compared to FIREcorr below 0.2 km) is affected by additional NOx and VOCs from the fires.

Quantitatively, the percentage contribution from fire emissions is calculated by (FIREcorr-CTRL)/FIREcorr during daytime over Huntsville. Fire emissions contribute 14% to the highest daytime PO_3 on 12 November (2 ppb out of 17 ppb at 1.6 km) and 25% on 13 November (5 ppb out of 19 ppb at 0.5 km). This different photochemical production is associated with variable fire emissions and different smoke transport patterns and meteorological conditions. At the surface, fire emissions contribute to the daytime ΔO_3 with 37% (7 ppb/10 hrs out of 18 ppb/10 hrs) on 12 November and with 30% (8 ppb/10 hrs out of 25 ppb/10 hrs) on 13 November, respectively. In the upper air, the relative contribution increases up to 44–58%. The smoke strength is indicated here by the fire-impacted $PM_{2.5}$. At the surface, fire emissions contribute to hourly $PM_{2.5}$ with 44% (12 $\mu g/m^3$ out of 27 $\mu g/m^3$) on 12 November and with 70% (32 $\mu g/m^3$ out of 47 $\mu g/m^3$) on 13 November. In the upper air, the relative contribution increases up to 51–77%. The results suggest an increased fire contribution to the enhancement of ozone and particulate matter from the surface to the upper air and from one day to the next.

Diurnal variability of process tendencies can be affected by the boundary layer evolution, transport changes over the course of the day, and photochemistry. To examine how the different processes vary over the day, we analyze the total and fire-impacted process tendencies for 7–9 LT, 11–13 LT, and 15–17 LT in Figure 12. The total PO_3 clearly peaks in the mid-day. The total advection term dominates in the late afternoon on 12 November and the middle of the day on 13 November when the largest inflow of ozone occurred. The total vertical mixing process is strongest when the PBL is built up in the middle of the day, and it dominates the surface ozone accumulation by dispersing upper air ozone downward.

The diurnal variability of the total tendency terms can help explain what processes drive the fire-related ozone increase during different times of the day. On 12 November, the transport process in the late afternoon drives the largest fire impacts on O_3 accumulation ($\sim$4 ppb/2 hrs near the surface), which is associated with the freshly emitted smoke plume discussed. Fire-impacted PO_3 from morning to mid-day is small, yet local net chemical production dominates the ozone increase in the elevated smoke plume. On 13 November, the largest ozone increase ($>$ 4 ppb/2 hrs) in the mid-day is dominated by local photochemistry, followed by stong vertical mixing as well as inflow of O_3 from fire emissions. This combined effect of net chemical production, transport, and vertical mixing on O_3 accumulation is most pronounced in mid-day when fire smoke impacted the boundary layer.

3.6 Uncertainties and Limitations

In this study, turning off the aerosol-radiation feedback in WRF-Chem ensures identical meteorology between the sensitivity simulations. We acknowledge that excluding the feedback may influence modeled ozone photochemistry. To address uncertainties induced by excluding the direct radiative effect, three additional sensitivity simulations (CTRL', FIREorig', and FIREcorr') are performed with the aerosol-radiation feedback turned on. Figure S10 shows results for photolysis rates for NO_2 ($J(NO_2)$) during the daytime on 12 and 13 November 2016. $J(NO_2)$ is shown as an indicator for the rate-limiting step in the photochemical formation of ozone (Baylon et al., 2018). In addition, fire-impacted $PM_{2.5}$ is used as an indicator for smoke altitude and magnitude. The daytime mean $J(NO_2)$ in the three different simulations (yellow lines) shows that increasing aerosol emissions tends to slightly increase $J(NO_2)$ at the top and above the smoke plumes, while decrease $J(NO_2)$ in the middle to the bottom parts of the plumes. The strongest suppression of $J(NO_2)$ appears at the bottom part of the plume. These results suggest that the additional smoke aerosols lead to a change in the vertical structure of the photochemical ozone formation, consistent with previous studies (Alvarado et al., 2015). Quantitatively, increasing fire aerosol emissions from the fires reduces surface $J(NO_2)$ by as much as -4% and -13% on 12 and 13 November (red lines in Figure S10), respectively. This change in actinic flux suggests that underestimation or overestimation of photochemical ozone production largely depends on the altitude with respect to smoke plumes for a given fire event. Our sensitivity simulation suggests that, by excluding the aerosol-radiation feedback, daytime ozone at the surface might be overestimated by 4% and 13% on 12 and 13 November, respectively. A slight overestimation in the plume center and a slight underestimation above the plume may result from excluding the feedback. Jiang et al. (2012) examined the direct radiative effects on ozone production for large-scale fires. Their results show that the reduction in both downward shortwave radiation and surface temperature can decrease both $J(NO_2)$ as well as biogenic isoprene emissions, resulting in reductions in surface ozone concentrations by as much as 15%.

Our analysis has limitations due to excluding secondary organic aerosol (SOA) and heterogeneous/aqueous chemistry in the MOZCART scheme. The formation of SOA in smoke plumes is highly variable; SOA can increase as the plume ages while in other cases can stay constant or even decrease (Akagi et al., 2012; Wigder et al., 2013; Alvarado et al., 2015). In a recent model study for the 2016 SEUS wildfires, Guan et al. (2020) have shown that SOA from fires accounts for 9% and 12% of $PM_{2.5}$ components for 6–9 November and 13–16 November, respectively. Therefore, considering SOA, our adjustment factor of aerosol emissions might be reduced from 3.6 to $\sim$3.2. Future studies are needed to estimate the additional uncertainties to the simulated AOD but are not expected to significantly alter our conclusions, namely that a factor of 3–4 is needed to scale the FINNv1.5 aerosol emissions for this fire event. Heterogeneous chemistry in aerosols and clouds may also affect the ozone budget in different ways. Although there is little evidence for significant heterogeneous ozone loss, the uptake of HO_2 and N_2O_5 by aqueous aerosols represents a potential sink (Jacob, 2000). A comparison between the most recently added T1_MOZCART and the MOZCART scheme used here shows that T1_MOZCART generally simulates somewhat lower surface ozone than MOZCART (https://www2.acom.ucar.edu/wrf-chem), and this change is mostly attributed to the inclusion of heterogeneous reactions on aerosols in T1 (Emmons et al., 2020). Although the results may differ when simulating other regions or times, we do not expect that the omission of heterogeneous chemistry will significantly alter our results. In addition, ceilometer measurement and satellite images show that the sky over Huntsville during our study period is mostly clear except for a short-time cloudy condition on the morning of 13 November. Therefore, we expect small impact on local ozone results from cloud chemistry for this specific case study.

4 Conclusions

Analyzing measurements from ozonesonde, O_3 DIAL, ceilometer, surface monitors, and space-borne observations together with the regional chemical transport model WRF-Chem provides evidence of wildfire impacts on the vertical distribution of ozone and aerosols over Huntsville, AL. Diagnostic analysis characterizes the relative roles of chemical and dynamical processes in the vertical ozone budget in fire smoke. Multi-platform observations are shown to be essential to evaluate the model performance from regional to local scale. This study uniquely combines the TOLNet/RO_3QET UV O_3 DIAL aerosol extinction product with MODIS AOD and EPA $PM_{2.5}$ concentrations to compare with the modeled smoke during a high particulate pollution episode of the 2016 SEUS wildfires.

During the daytime on 12 and 13 November 2016, fire emissions contribute 12–32 $\mu g/m^3$ (40–70%) to hourly surface $PM_{2.5}$ at Huntsville and dominate the local particulate air pollution on 13 November. Besides the freshly emitted smoke plumes, relatively aged plumes emitted from previous days contribute considerably to the entire PBL $PM_{2.5}$ accumulation. Fire emissions contribute 7–8 ppb/10 hrs (30–37%) to the daytime surface ozone increase at Huntsville. Although O_3 is of less concern for air quality during this fire episode because concentrations remained below national health standards, investigating the fire influence mechanism on the vertical ozone budget provides insights into the variability of the ozone distribution downstream of wildfires. In particular, the main sources of fire-impacted ΔO_3 are demonstrated by sensitivity simulations and tendency diagnostics: (1) Fire emissions increase the vertical ozone concentrations downstream of the fires by affecting the local net chemical ozone production, inflow and outflow of ozone, and the vertical ozone exchange. These processes vary in importance on daily, diurnal, and vertical scales. On 12 November, local net photochemical ozone production over Huntsville dominates the fire-impacted ozone enhancement in the elevated plume while transport processes dominate the boundary layer ozone accumulation in the late afternoon. On 13 November, local net photochemical ozone production dominates the fire-impacted ozone enhancement below 1 km. (2) Local net chemical production of ozone from biomass burning was not the dominant source of surface ozone these days. However, the vertical mixing and advection of ozone produced elsewhere from biomass burning emissions enhanced the overall impacts of biomass burning on local ozone. The combined effect of chemical and dynamical processes leads to a percentage contribution to ΔO_3 of 30–37% at the surface and up to 44–58% in the upper air.

For the considered case studies, WRF-Chem captures the general day-to-day AOD pattern, air-quality variations, vertical structure of aged plumes, and enhanced ozone lamina. Three main avenues for future work follow from our work: (1) Discrepancies in fire emission estimations need to be considered for model inputs. The (OC+BC)/CO emission ratios in FINNv1.5, GFEDv4s, GFASv1.2, and QFEDv2.5_r1 fire inventories differ by a factor of 5.7 (in Gg per Gg) over the 2016 SEUS wildfire region. A scaling ratio of 3–4 on aerosol emissions (derived from FINNv1.5 $PM_{2.5}$ and PM_{10}), within the spanned range of the emission ratios in different inventories, was needed in our case to improve the modeled magnitude of surface $PM_{2.5}$, vertical aerosol extinction, and AOD. (2) After the emission adjustment, the underestimation of the densest plume in DIAL and highest AOD in MODIS is partly due to missing fire detections under clouds on 13 November. Adding extra satellite detections (e.g., FINNv2.2 includes VIIRS information) or filling in the gap of missing fire counts in emission estimation algorithms should be considered; (3) The density, continuity, and species of vertical measurements are relatively limited for modeling evaluation. Available larger samples of vertical measurements (ground-based and airborne) with ambient data will benefit regional-model evaluation in future fire studies.

In summary, our results reveal the different mechanisms by which fires can influence the vertical ozone budget downstream of the wildfires and point out large uncer-

tainties in fire emissions. Our case study reveals the benefits of combining observations from multiple platforms for characterizing fire impacts on surface and upper air chemical composition and for the in-depth evaluation of models. Albeit ozone concentrations during the considered fire episode were of less concern for air quality management, our analysis of the ozone budget in fire smoke provides valuable insight into the complex interplay of chemical and dynamical processes. Future work combining modeling diagnostic tools with a larger sample of ground-based and airborne measurements for a multitude of fire episodes is needed to gain a more generalized understanding of the ozone evolution in wildfire plumes and subsequent air-quality and policy implications.

Acknowledgments

The authors thank three anonymous reviewers for providing constructive comments. This work was supported by the TOLNet program developed by National Aeronautics and Space Administration (NASA)'s Science Mission Directorate, and the National Center for Atmospheric Research (NCAR), which is a major facility sponsored by the National Science Foundation under Cooperative Agreement No. 1852977. The views, opinions, and findings contained in this work are those of the authors and should not be construed as an official position, policy, or decision. We acknowledge use of the WRF-Chem preprocessor tools provided by the Atmospheric Chemistry Observations and Modeling Lab (ACOM) of NCAR. We appreciate the developers of the FINNv1.5, GFASv1.2, GFEDv4s and QFEDv2.5_r1 fire inventories. We acknowledge the use of imagery from the NASA Worldview application (https://worldview.earthdata.nasa.gov), part of the NASA Earth Observing System Data and Information System (EOSDIS). The authors would like to thank Kevin Knupp and Dustin Phillips for providing ceilometer data, Michael Graham for launching the ozonesonde, and Peiyang Cheng for extracting surface air-quality data in model evaluation. Helpful discussions with Udaysankar Nair, Zhixin Xue, Andrew White, Paula Tucker, Yonghua Wu, and the ACOM lab are gratefully acknowledged. The ceilometer datasets used in this study are archived at https://www.nsstc.uah.edu/mips/data/data/. The ozonesonde and DIAL datasets in this study are available at https://doi.org/10.5281/zenodo.4019663. Surface ozone and $PM_{2.5}$ datasets are downloaded from the Environmental Protection Agency (EPA) website (https://www.epa.gov/outdoor-air-quality-data). MODIS aerosol optical depth data is acquired from the NASA Earth Data Level-1 and Atmospheric Archive & Distribution System Distributed Active Archive Center (LAADS DAAC) website via https://ladsweb.modaps.eosdis.nasa.gov/. The WRF-Chem preprocessor tools and emission inputs used in this study are available via https://www2.acom.ucar.edu/wrf-chem/wrf-chem-tools-community.

Table 1. Key Configurations for the WRF-Chem v3.9.1 Simulations

Simulations	1. CTRL (fire off)	2. FIREorig (fire on)	3. FIREcorr (fire on, correction)
Vertical	60 vertical levels from the surface to 50 hPa (vertical grids in Figure S1)		
Horizontal	D01: 16 km×16 km, D02: 4 km×4 km		
Emissions	Fire: FINNv1.5, Anthropogenic: NEI 2011 v2, Biogenic: MEGAN		
IC&BC	Met: NAM 12 km, Chemical: MOZART global		
Chemistry	MOZART gas, GOCART aerosol		
Physics	Goddard, RRTM, Morrison's, Monin-Obukhov, Noah, YSU, G3, F-TUV		

References

Akagi, S. K., Craven, J., Taylor, J., McMeeking, G., Yokelson, R., Burling, I., ... others (2012). Evolution of trace gases and particles emitted by a chaparral fire in california. *Atmospheric Chemistry and Physics*, *12*(3), 1397–1421.

Akagi, S. K., Yokelson, R. J., Wiedinmyer, C., Alvarado, M. J., Reid, J. S., Karl, T., ... Wennberg, P. O. (2011). Emission factors for open and domestic biomass burning for use in atmospheric models. *Atmospheric Chemistry and Physics*, *11*(9), 4039–4072. doi: 10.5194/acp-11-4039-2011

Alvarado, M., Lonsdale, C., Yokelson, R., Akagi, S. K., Coe, H., Craven, J., ... others (2015). Investigating the links between ozone and organic aerosol chemistry in a biomass burning plume from a prescribed fire in california chaparral. *Atmospheric Chemistry and Physics*, *15*(12), 6667–6688.

Andreae, M. O., & Merlet, P. (2001). Emission of trace gases and aerosols from biomass burning. *Global biogeochemical cycles*, *15*(4), 955–966.

Aouizerats, B., Van Der Werf, G. R., Balasubramanian, R., & Betha, R. (2015). Importance of transboundary transport of biomass burning emissions to regional air quality in southeast asia during a high fire event. *Atmospheric Chemistry & Physics*, *15*(1).

Baker, K., Woody, M., Tonnesen, G., Hutzell, W., Pye, H., Beaver, M., ... Pierce, T. (2016). Contribution of regional-scale fire events to ozone and pm2. 5 air quality estimated by photochemical modeling approaches. *Atmospheric Environment*, *140*, 539–554.

Baker, K., Woody, M., Valin, L., Szykman, J., Yates, E., Iraci, L., ... others (2018). Photochemical model evaluation of 2013 california wild fire air quality impacts using surface, aircraft, and satellite data. *Science of the Total Environment*, *637*, 1137–1149.

Barth, M., Lee, J., Hodzic, A., Pfister, G., Skamarock, W., Worden, J., ... Noone, D. (2012). Thunderstorms and upper troposphere chemistry during the early stages of the 2006 north american monsoon. *Atmospheric Chemistry & Physics*, *12*(22).

Baylon, P., Jaffe, D., Hall, S., Ullmann, K., Alvarado, M., & Lefer, B. (2018). Impact of biomass burning plumes on photolysis rates and ozone formation at the mount bachelor observatory. *Journal of Geophysical Research: Atmospheres*, *123*(4), 2272–2284.

Carter, T. S., Heald, C. L., Jimenez, J. L., Campuzano-Jost, P., Kondo, Y., Moteki, N., ... others (2020). How emissions uncertainty influences the distribution and radiative impacts of smoke from fires in north america. *Atmospheric Chemistry and Physics*, *20*(4), 2073–2097.

Chin, M., Rood, R. B., Lin, S.-J., Müller, J.-F., & Thompson, A. M. (2000). Atmospheric sulfur cycle simulated in the global model gocart: Model description and global properties. *Journal of Geophysical Research: Atmospheres*, *105*(D20), 24671–24687.

Colarco, P., Schoeberl, M., Doddridge, B., Marufu, L., Torres, O., & Welton, E. (2004). Transport of smoke from canadian forest fires to the surface near washington, dc: Injection height, entrainment, and optical properties. *Journal of Geophysical Research: Atmospheres*, *109*(D6).

Cook, P. A., Savage, N. H., Turquety, S., Carver, G. D., O'Connor, F. M., Heckel, A., ... others (2007). Forest fire plumes over the north atlantic: p-tomcat model simulations with aircraft and satellite measurements from the itop/icartt campaign. *Journal of Geophysical Research: Atmospheres*, *112*(D10).

Cooper, O. R., Langford, A. O., Parrish, D. D., & Fahey, D. W. (2015). Challenges of a lowered us ozone standard. *Science*, *348*(6239), 1096–1097.

Crutzen, P. J., & Andreae, M. O. (1990). Biomass burning in the tropics: Impact on atmospheric chemistry and biogeochemical cycles. *Science*, *250*(4988), 1669–

1678.

Crutzen, P. J., Heidt, L. E., Krasnec, J. P., Pollock, W. H., & Seiler, W. (1979). Biomass burning as a source of atmospheric gases co, h2, n2o, no, ch3cl and cos. *Nature*, *282*(5736), 253.

Curci, G., Hogrefe, C., Bianconi, R., Im, U., Balzarini, A., Baró, R., ... others (2015). Uncertainties of simulated aerosol optical properties induced by assumptions on aerosol physical and chemical properties: An aqmeii-2 perspective. *Atmospheric Environment*, *115*, 541–552.

Darmenov, A., & da Silva, A. (2013). The quick fire emissions dataset (qfed)–documentation of versions 2.1, 2.2 and 2.4. *NASA Technical Report Series on Global Modeling and Data Assimilation, NASA TM-2013-104606*, *32*, 183.

Emmons, L., Schwantes, R. H., Orlando, J. J., Tyndall, G., Kinnison, D., Lamarque, J.-F., ... Pétron, G. (2020). The chemistry mechanism in the community earth system model version 2 (cesm2). *Journal of Advances in Modeling Earth Systems*, *12*(4), e2019MS001882.

Emmons, L., Walters, S., Hess, P., Lamarque, J., Pfister, G., Fillmore, D., ... others (2010). *Description and evaluation of the model for ozone and related chemical tracers, version 4 (mozart-4), geosci. model dev., 3, 43–67.*

Fast, J. D., Gustafson Jr, W. I., Easter, R. C., Zaveri, R. A., Barnard, J. C., Chapman, E. G., ... Peckham, S. E. (2006). Evolution of ozone, particulates, and aerosol direct radiative forcing in the vicinity of houston using a fully coupled meteorology-chemistry-aerosol model. *Journal of Geophysical Research: Atmospheres*, *111*(D21).

Fiore, A. M., Pierce, R. B., Dickerson, R. R., Lin, M., & Bradley, R. (2014). Detecting and attributing episodic high background ozone events. *AQAST Special Issue of Environmental Manager*.

Freitas, S. R., Longo, K. M., Chatfield, R., Latham, D., Silva Dias, M., Andreae, M., ... Carvalho Jr, J. (2007). Including the sub-grid scale plume rise of vegetation fires in low resolution atmospheric transport models. *Atmospheric Chemistry and Physics*, *7*(13), 3385–3398.

Giglio, L., Randerson, J. T., & Van Der Werf, G. R. (2013). Analysis of daily, monthly, and annual burned area using the fourth-generation global fire emissions database (gfed4). *Journal of Geophysical Research: Biogeosciences*, *118*(1), 317–328.

Grell, G. A., Peckham, S. E., Schmitz, R., McKeen, S. A., Frost, G., Skamarock, W. C., & Eder, B. (2005). Fully coupled "online" chemistry within the wrf model. *Atmospheric Environment*, *39*(37), 6957–6975.

Gronoff, G., Robinson, J., Berkoff, T., Swap, R., Farris, B., Schroeder, J., ... others (2019). A method for quantifying near range point source induced o3 titration events using co-located lidar and pandora measurements. *Atmospheric Environment*, *204*, 43–52.

Guan, S., Wong, D. C., Gao, Y., Zhang, T., & Pouliot, G. (2020). Impact of wildfire on particulate matter in the southeastern united states in november 2016. *Science of The Total Environment*, 138354.

Guenther, A., Karl, T., Harley, P., Wiedinmyer, C., Palmer, P., & Geron, C. (2006). Estimates of global terrestrial isoprene emissions using megan (model of emissions of gases and aerosols from nature). *Atmospheric Chemistry and Physics*, *6*(11), 3181–3210.

Hodzic, A., Madronich, S., Bohn, B., Massie, S., Menut, L., & Wiedinmyer, C. (2007). Wildfire particulate matter in europe during summer 2003: meso-scale modeling of smoke emissions, transport and radiative effects. *Atmospheric Chemistry and Physics*, *7*(15), 4043–4064.

Hu, X.-M., Xue, M., Kong, F., & Zhang, H. (2019). Meteorological conditions during an ozone episode in dallas-fort worth, texas, and impact of their modeling uncertainties on air quality prediction. *Journal of Geophysical Research:*

Atmospheres, *124*(4), 1941–1961.

Jacob, D. J. (2000). Heterogeneous chemistry and tropospheric ozone. *Atmospheric Environment*, *34*(12-14), 2131–2159.

Jaffe, D., Bertschi, I., Jaeglé, L., Novelli, P., Reid, J. S., Tanimoto, H., ... Westphal, D. L. (2004). Long-range transport of siberian biomass burning emissions and impact on surface ozone in western north america. *Geophysical Research Letters*, *31*(16).

Jaffe, D., Wigder, N., Downey, N., Pfister, G., Boynard, A., & Reid, S. B. (2013). Impact of wildfires on ozone exceptional events in the western us. *Environmental science & technology*, *47*(19), 11065–11072.

Jiang, X., Wiedinmyer, C., & Carlton, A. G. (2012). Aerosols from fires: An examination of the effects on ozone photochemistry in the western united states. *Environmental science & technology*, *46*(21), 11878–11886.

Johnson, B., Oltmans, S. J., Vömel, H., Smit, H. G., Deshler, T., & Kröger, C. (2002). Electrochemical concentration cell (ecc) ozonesonde pump efficiency measurements and tests on the sensitivity to ozone of buffered and unbuffered ecc sensor cathode solutions. *Journal of Geophysical Research: Atmospheres*, *107*(D19), ACH–8.

Johnson, M., Kuang, S., Wang, L., & Newchurch, M. (2016). Evaluating summertime ozone enhancement events in the southeast united states. *Atmosphere*, *7*(8), 108.

Johnson, M., Strawbridge, K., Knowland, K. E., Keller, C., & Travis, M. (2021). Long-range transport of siberian biomass burning emissions to north america during firex-aq. *Atmospheric Environment*, 118241.

Justice, C., Giglio, L., Korontzi, S., Owens, J., Morisette, J., Roy, D., ... Kaufman, Y. (2002). The modis fire products. *Remote Sensing of Environment*, *83*(1-2), 244–262.

Kaiser, J., Heil, A., Andreae, M., Benedetti, A., Chubarova, N., Jones, L., ... others (2012). Biomass burning emissions estimated with a global fire assimilation system based on observed fire radiative power. *Biogeosciences*, *9*(1), 527–554.

Konrad, C., & Knox, P. (2017). *The southeastern drought and wildfires of 2016* (Tech. Rep.). The Southeast Regional Climate Center (SERCC). Retrieved from `https://sercc.com/NIDISDroughtAssessmentFINAL.pdf`

Kuang, S., Burris, J. F., Newchurch, M. J., Johnson, S., & Long, S. (2011). Differential absorption lidar to measure subhourly variation of tropospheric ozone profiles. *IEEE Transactions on Geoscience and Remote Sensing*, *49*(1), 557–571.

Kuang, S., Newchurch, M. J., Johnson, M. S., Wang, L., Burris, J., Pierce, R. B., ... Feng, N. (2017, Jan). Summertime tropospheric ozone enhancement associated with a cold front passage due to stratosphere-to-troposphere transport and biomass burning: Simultaneous ground-based lidar and airborne measurements. *Journal of Geophysical Research (Atmospheres)*, *122*(2), 1293-1311. doi: 10.1002/2016JD026078

Kuang, S., Wang, B., Newchurch, M. J., Tucker, P., Eloranta, E. W., Garcia, J. P., ... others (2020). Evaluation of uv aerosol retrievals from an ozone lidar. *Atmospheric Measurement Techniques Discussions*, 1–20.

Langford, A. O., Alvarez, I., Raul, J., Kirgis, G., Senff, C. J., Caputi, D., ... others (2019). Intercomparison of lidar, aircraft, and surface ozone measurements in the san joaquin valley during the california baseline ozone transport study (cabots). *Atmospheric Measurement Techniques*, *12*(3), 1889–1904.

Langford, A. O., Alvarez, R. J., Brioude, J., Caputi, D., Conley, S. A., Evan, S., ... others (2020). Ozone production in the soberanes smoke haze: implications for air quality in the san joaquin valley during the california baseline ozone transport study. *Journal of Geophysical Research: Atmospheres*, *125*(11), e2019JD031777.

Langford, A. O., Alvarez II, R., Brioude, J., Evan, S., Iraci, L., Kirgis, G., ... others (2018). Coordinated profiling of stratospheric intrusions and transported pollution by the tropospheric ozone lidar network (tolnet) and nasa alpha jet experiment (ajax): Observations and comparison to hysplit, raqms, and flexpart. *Atmospheric environment*, *174*, 1–14.

Langford, A. O., Senff, C., Alvarez Ii, R., Brioude, J., Cooper, O., Holloway, J., ... others (2015). An overview of the 2013 las vegas ozone study (lvos): Impact of stratospheric intrusions and long-range transport on surface air quality. *Atmospheric environment*, *109*, 305–322.

Lapina, K., Honrath, R., Owen, R., Val Martin, M., & Pfister, G. (2006). Evidence of significant large-scale impacts of boreal fires on ozone levels in the midlatitude northern hemisphere free troposphere. *Geophysical Research Letters*, *33*(10).

Leblanc, T., Brewer, M. A., Wang, P. S., & Granados Muñoz, M. J. (2018). Validation of the tolnet lidars: the southern california ozone observation project (scoop). *Atmospheric measurement techniques*, *11*, 6137–6162.

Levy, R., Hsu, C., et al. (2015). *Modis atmosphere l2 aerosol product, nasa modis adaptive processing system, goddard space flight center, usa.*

Lindaas, J., Farmer, D. K., Pollack, I. B., Abeleira, A., Flocke, F., Roscioli, R., ... Fischer, E. V. (2017). Changes in ozone and precursors during two aged wildfire smoke events in the colorado front range in summer 2015. *Atmospheric Chemistry and Physics*, *17*(17), 10691–10707.

Liu, T., Mickley, L. J., Marlier, M. E., DeFries, R. S., Khan, M. F., Latif, M. T., & Karambelas, A. (2020). Diagnosing spatial biases and uncertainties in global fire emissions inventories: Indonesia as regional case study. *Remote Sensing of Environment*, *237*, 111557.

Lu, X., Zhang, L., Liu, X., Gao, M., Zhao, Y., & Shao, J. (2018). Lower tropospheric ozone over india and its linkage to the south asian monsoon. *Atmospheric Chemistry and Physics*, *18*(5), 3101–3118.

Martin, M. V., Honrath, R., Owen, R. C., Pfister, G., Fialho, P., & Barata, F. (2006). Significant enhancements of nitrogen oxides, black carbon, and ozone in the north atlantic lower free troposphere resulting from north american boreal wildfires. *Journal of Geophysical Research: Atmospheres*, *111*(D23).

McKeen, S., Wotawa, G., Parrish, D., Holloway, J., Buhr, M., Hübler, G., ... Meagher, J. (2002). Ozone production from canadian wildfires during june and july of 1995. *Journal of Geophysical Research: Atmospheres*, *107*(D14), ACH–7.

Morris, G. A., Hersey, S., Thompson, A. M., Pawson, S., Nielsen, J. E., Colarco, P. R., ... others (2006). Alaskan and canadian forest fires exacerbate ozone pollution over houston, texas, on 19 and 20 july 2004. *Journal of Geophysical Research: Atmospheres*, *111*(D24).

Newchurch, M., Ayoub, M., Oltmans, S., Johnson, B., & Schmidlin, F. (2003). Vertical distribution of ozone at four sites in the united states. *Journal of Geophysical Research: Atmospheres*, *108*(D1).

Oltmans, S., Lefohn, A., Harris, J., Tarasick, D., Thompson, A., Wernli, H., ... others (2010). Enhanced ozone over western north america from biomass burning in eurasia during april 2008 as seen in surface and profile observations. *Atmospheric Environment*, *44*(35), 4497–4509.

Pereira, G., Siqueira, R., Rosário, N. E., Longo, K. L., Freitas, S. R., Cardozo, F. S., ... Wooster, M. J. (2016). Assessment of fire emission inventories during the south american biomass burning analysis (sambba) experiment. *Atmospheric Chemistry and Physics*.

Pfister, G., Avise, J., Wiedinmyer, C., Edwards, D., Emmons, L., Diskin, G., ... Wisthaler, A. (2011). Co source contribution analysis for california during arctas-carb. *Atmospheric Chemistry and Physics*, *11*(15), 7515–7532.

Pfister, G., Wang, C.-T., Barth, M., Flocke, F., Vizuete, W., & Walters, S. (2019). Chemical characteristics and ozone production in the northern colorado front range. *Journal of Geophysical Research: Atmospheres*.

Pfister, G., Wiedinmyer, C., & Emmons, L. (2008). Impacts of the fall 2007 california wildfires on surface ozone: Integrating local observations with global model simulations. *Geophysical Research Letters*, *35*(19).

Polivka, T. N., Wang, J., Ellison, L. T., Hyer, E. J., & Ichoku, C. M. (2016). Improving nocturnal fire detection with the viirs day–night band. *IEEE Transactions on Geoscience and Remote Sensing*, *54*(9), 5503–5519.

Randerson, J., Chen, Y., Van Der Werf, G., Rogers, B., & Morton, D. (2012). Global burned area and biomass burning emissions from small fires. *Journal of Geophysical Research: Biogeosciences*, *117*(G4).

Reid, J. S., Kuehn, R. E., Holz, R. E., Eloranta, E. W., Kaku, K. C., Kuang, S., ... others (2017). Ground-based high spectral resolution lidar observation of aerosol vertical distribution in the summertime southeast united states. *Journal of Geophysical Research: Atmospheres*, *122*(5), 2970–3004.

Rogers, H. M., Ditto, J. C., & Gentner, D. R. (2020). Evidence for impacts on surface-level air quality in the northeastern us from long-distance transport of smoke from north american fires during the long island sound tropospheric ozone study (listos) 2018. *Atmospheric Chemistry and Physics*, *20*(2), 671–682.

Sapkota, A., Symons, J. M., Kleissl, J., Wang, L., Parlange, M. B., Ondov, J., ... Buckley, T. J. (2005). Impact of the 2002 canadian forest fires on particulate matter air quality in baltimore city. *Environmental science & technology*, *39*(1), 24–32.

Strawbridge, K. B., Travis, M. S., Firanski, B. J., Brook, J. R., Staebler, R., & Leblanc, T. (2018). A fully autonomous ozone, aerosol and nighttime water vapor lidar: a synergistic approach to profiling the atmosphere in the canadian oil sands region. *Atmospheric Measurement Techniques*, *11*(12), 6735–6759.

Sullivan, J. T., Berkoff, T., Gronoff, G., Knepp, T., Pippin, M., Allen, D., ... others (2019). The ozone water–land environmental transition study: An innovative strategy for understanding chesapeake bay pollution events. *Bulletin of the American Meteorological Society*, *100*(2), 291–306.

Thompson, A. M., Oltmans, S. J., Tarasick, D. W., von der Gathen, P., Smit, H. G., & Witte, J. C. (2011). Strategic ozone sounding networks: Review of design and accomplishments. *Atmospheric Environment*, *45*(13), 2145–2163.

van der Werf, G. R., Randerson, J. T., Giglio, L., Van Leeuwen, T. T., Chen, Y., Rogers, B. M., ... others (2017). Global fire emissions estimates during 1997-2016. *Earth System Science Data*, *9*(2), 697–720.

Wang, J., Christopher, S. A., Nair, U., Reid, J. S., Prins, E. M., Szykman, J., & Hand, J. L. (2006). Mesoscale modeling of central american smoke transport to the united states: 1."top-down" assessment of emission strength and diurnal variation impacts. *Journal of Geophysical Research: Atmospheres*, *111*(D5).

Wang, J., Yue, Y., Wang, Y., Ichoku, C., Ellison, L., & Zeng, J. (2018). Mitigating satellite-based fire sampling limitations in deriving biomass burning emission rates: Application to wrf-chem model over the northern sub-saharan african region. *Journal of Geophysical Research: Atmospheres*, *123*(1), 507–528.

Wiedinmyer, C., Akagi, S., Yokelson, R. J., Emmons, L., Al-Saadi, J., Orlando, J., & Soja, A. (2011). The fire inventory from ncar (finn): a high resolution global model to estimate the emissions from open burning. *Geoscientific Model Development*, *4*(3), 625.

Wiegner, M., Madonna, F., Binietoglou, I., Forkel, R., Gasteiger, J., Geiß, A., ... Thomas, W. (2014). What is the benefit of ceilometers for aerosol remote sensing? an answer from earlinet. *Atmospheric Measurement Techniques*, *7*(7), 1979–1997.

Wigder, N., Jaffe, D., & Saketa, F. (2013). Ozone and particulate matter enhancements from regional wildfires observed at mount bachelor during 2004–2011. *Atmospheric Environment*, *75*, 24–31.

Williams, P., Cook, B. I., Smerdon, J. E., Bishop, D. A., Seager, R., & Mankin, J. S. (2017). The 2016 southeastern us drought: An extreme departure from centennial wetting and cooling. *Journal of Geophysical Research: Atmospheres*, *122*(20), 10–888.

Wingo, S. M., & Knupp, K. R. (2015). Multi-platform observations characterizing the afternoon-to-evening transition of the planetary boundary layer in northern alabama, usa. *Boundary-Layer Meteorology*, *155*(1), 29–53.

WRAP. (2005). (western regional air partnership): 2002 fire emission inventory for the wrap region-phase ii. *Project No. 178-6, available at: https://www.wrapair.org/forums/fejf/documents/WRAP_2002_PhII_EI_Report_20050722.pdf (last access: 17 January 2020)*.

Wu, Y., Han, Y., Voulgarakis, A., Wang, T., Li, M., Wang, Y., ... Li, S. (2017). An agricultural biomass burning episode in eastern china: Transport, optical properties, and impacts on regional air quality. *Journal of Geophysical Research: Atmospheres*, *122*(4), 2304–2324.

Zhang, F., Wang, J., Ichoku, C., Hyer, E. J., Yang, Z., Ge, C., ... others (2014). Sensitivity of mesoscale modeling of smoke direct radiative effect to the emission inventory: a case study in northern sub-saharan african region. *Environmental Research Letters*, *9*(7), 075002.

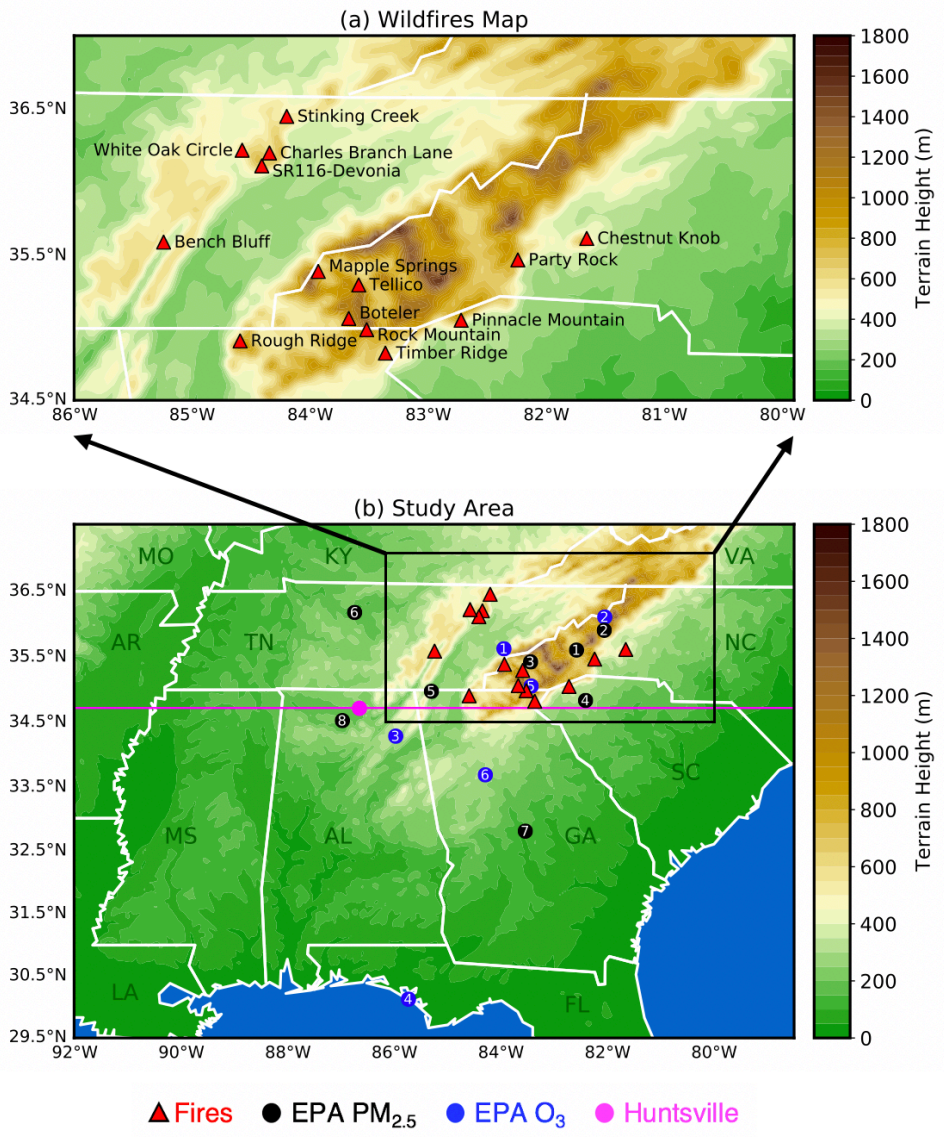

Figure 1. (a) Map of 14 active wildfires (red triangles) during 11–14 November, 2016 (see Table S1 for details). Here the names of wildfires are defined by the Monitoring Trends in Burn Severity project (MTBS; www.mtbs.gov). (b) WRF-Chem inner domain (D02) and terrain height (m). Black dots, blue dots, and magenta dot represent the 8 EPA $PM_{2.5}$ sites, 6 EPA O_3 sites, and Huntsville station, respectively. The magenta line in the inner model domain (D02) indicates the route of the vertical section in Figure 10.

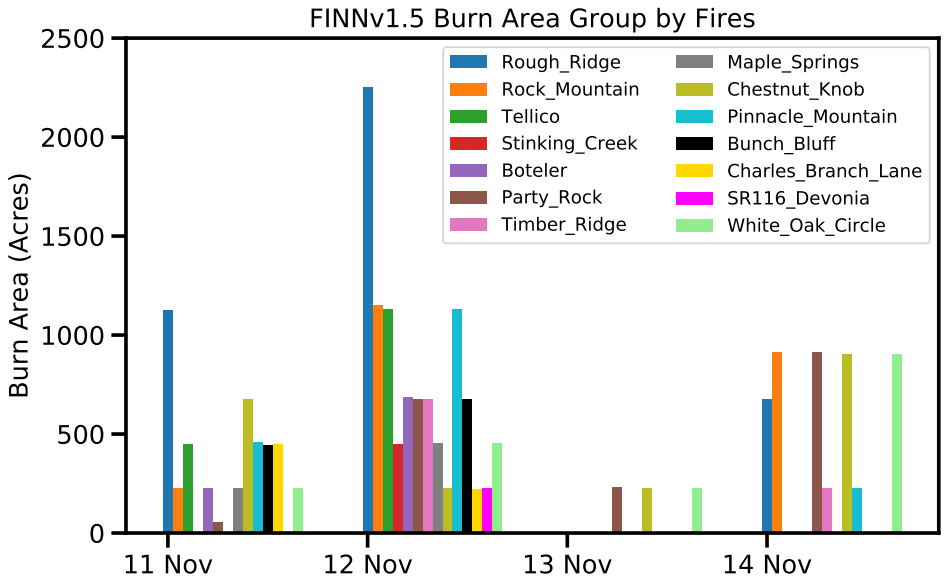

Figure 2. FINNv1.5 daily burn area (acres) group by individual wildfire during 11–14 November 2016. The daily burn area is aggregated in the geospatial boundary box of each wildfire that defined by MTBS database.

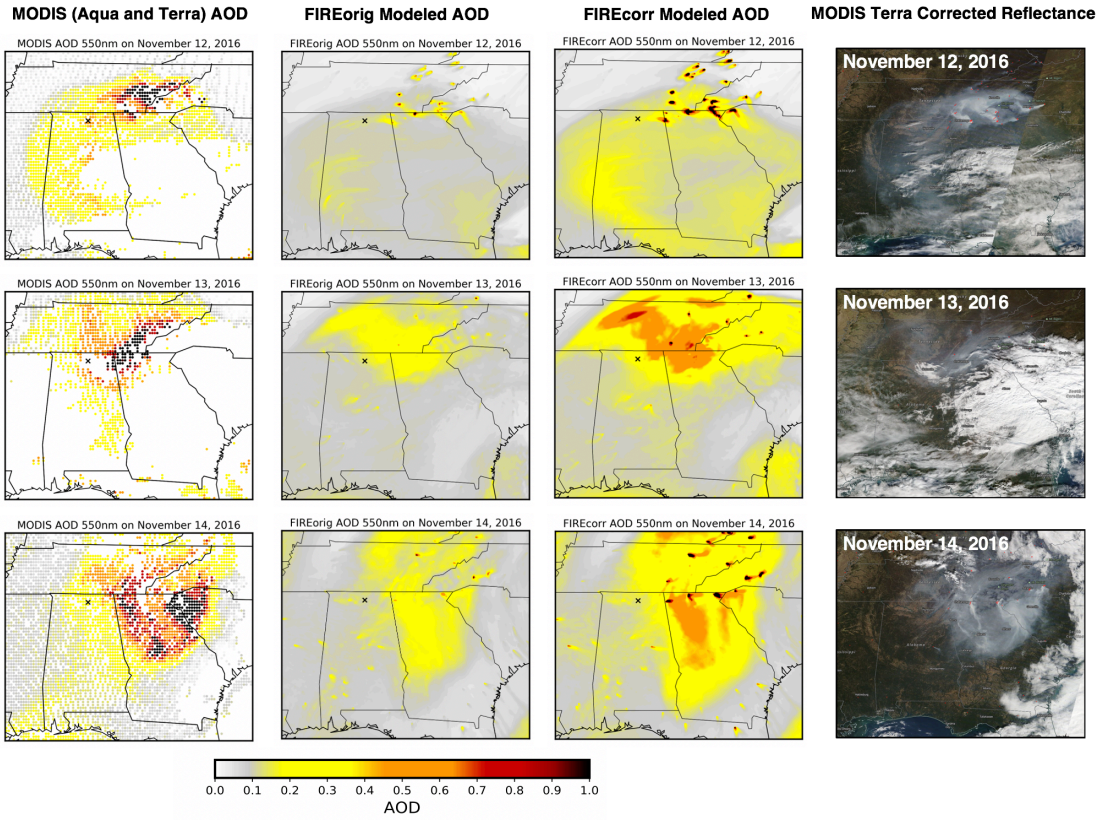

Figure 3. MODIS Vs. WRF-Chem AOD at 550 nm in SEUS region in 12–14 (Row 1–3) November 2016. Column 1 to 4 shows MODIS AOD, FIREorig AOD (before adjustment), FIREcorr AOD (after adjustment), and MODIS reflectance, respectively. Cross marker indicates Huntsville location. In the MODIS reflectance images, the red dots represent the fires and thermal anomalies product.

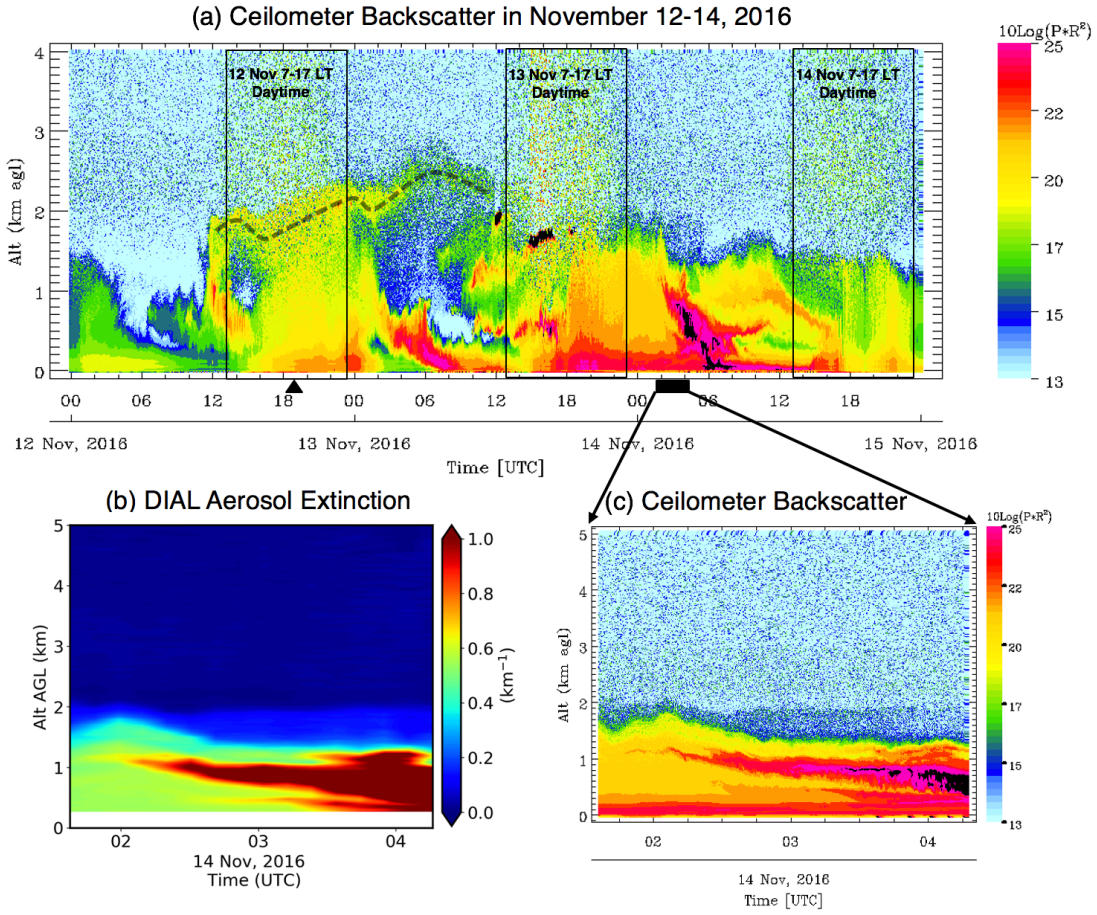

Figure 4. (a) Time-height curtain of UAH CT25K ceilometer backscatter intensity in 12–14 November 2016 (courtesy of Kevin Knupp). Here UTC time minus 6 hours is local time. The black triangle indicates the launch time of an ozonesonde. The black rectangle indicates the measurement time of DIAL. (b) Time-height curtain of DIAL aerosol extinction coefficient at 299 nm in 1:37–4:17 UTC on 14 November (19:37 to 22:17 LT 13 November). (c) Same time period with (b), but for ceilometer backscatter intensity at 905 nm.

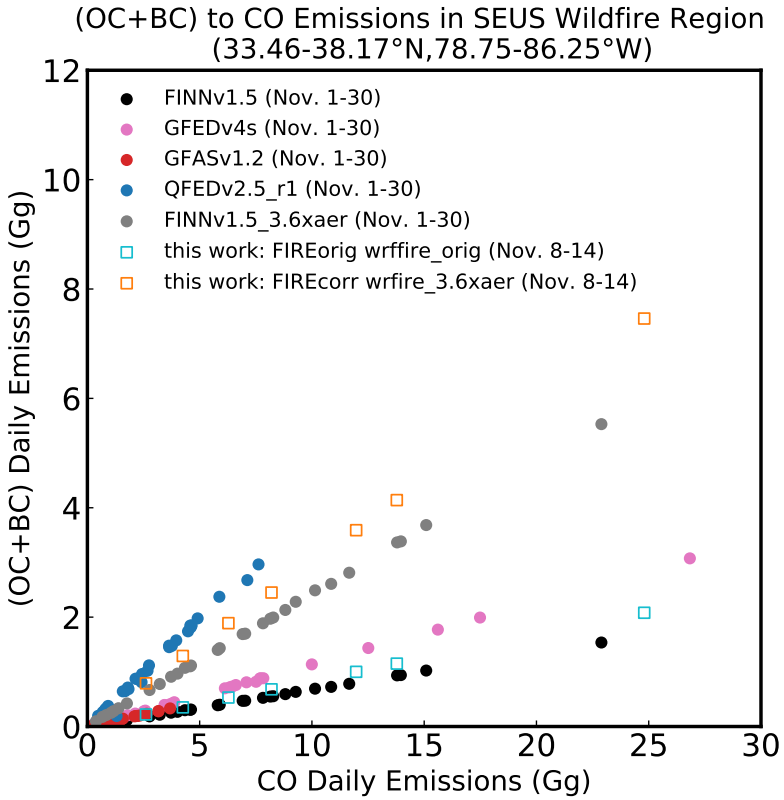

Figure 5. Comparison of fire emission ratios for (OC+BC) versus CO between this work and the different inventories. Daily emissions in the wildfire region are summed up within the latitude and longitude boundary 33.46–38.17° N and 78.75–86.25° W (Figure S4). The black, pink, red, and blue dots represent daily emissions in 1–30 November 2016 from FINNv1.5, GFEDv4s, GFASv1.2, and QFEDv2.5_r1 inventories, respectively. Unfilled aqua and orange squares represent daily emissions in 8–14 November 2016 from FIREorig and FIREcorr runs, respectively. The gray dots denote a scaling by 3.6 on the original FINNv1.5 aerosols for a reference. Note the recommended scaling factor 3.4 on GFASv1.2 aerosol emissions by Kaiser et al. (2012) is not shown in this plot.

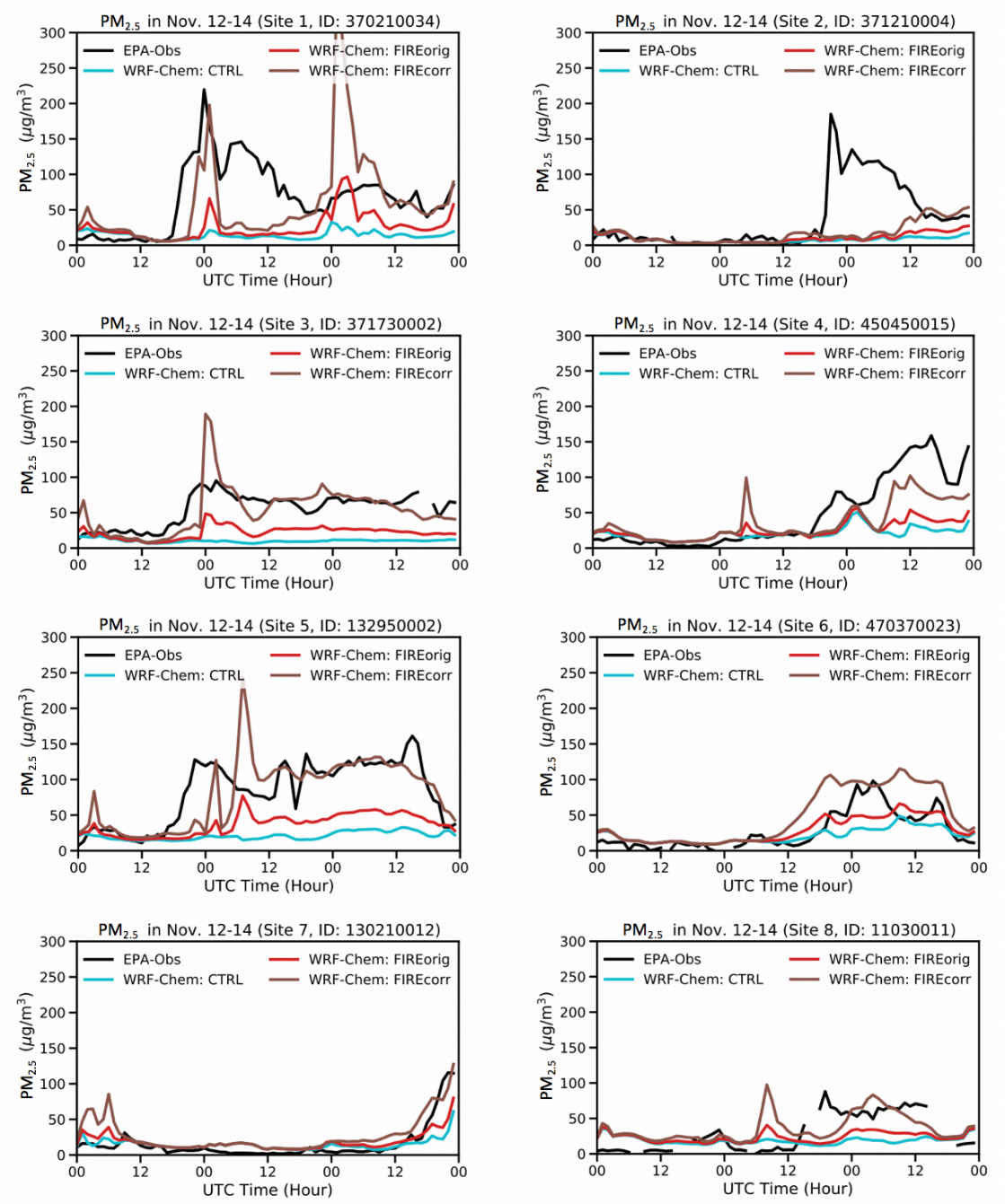

Figure 6. Comparison between 8 EPA sites (black line) and WRF-Chem hourly ~~PM2.5~~$PM_{2.5}$ in 12–14 November 2016 for control run CTRL (aqua), before the emissions adjustment FIREorig (red), and after the emissions adjustment FIREcorr (brown). The control run is performed to show the modeled $PM_{2.5}$ without fire impacts. Pattern statistic can be seen in Figure S5. 8 EPA $PM_{2.5}$ sites include: 1. Asheville, NC, 2. Mitchell, NC, 3. Swain, NC, 4. Greenville-Anderson-Mauldin, SC, 5. Chattanooga, TN-GA, 6. Nashville-Davidson-Murfreesboro-Franklin, TN, 7. Macon, GA, 8. Decatur, AL.

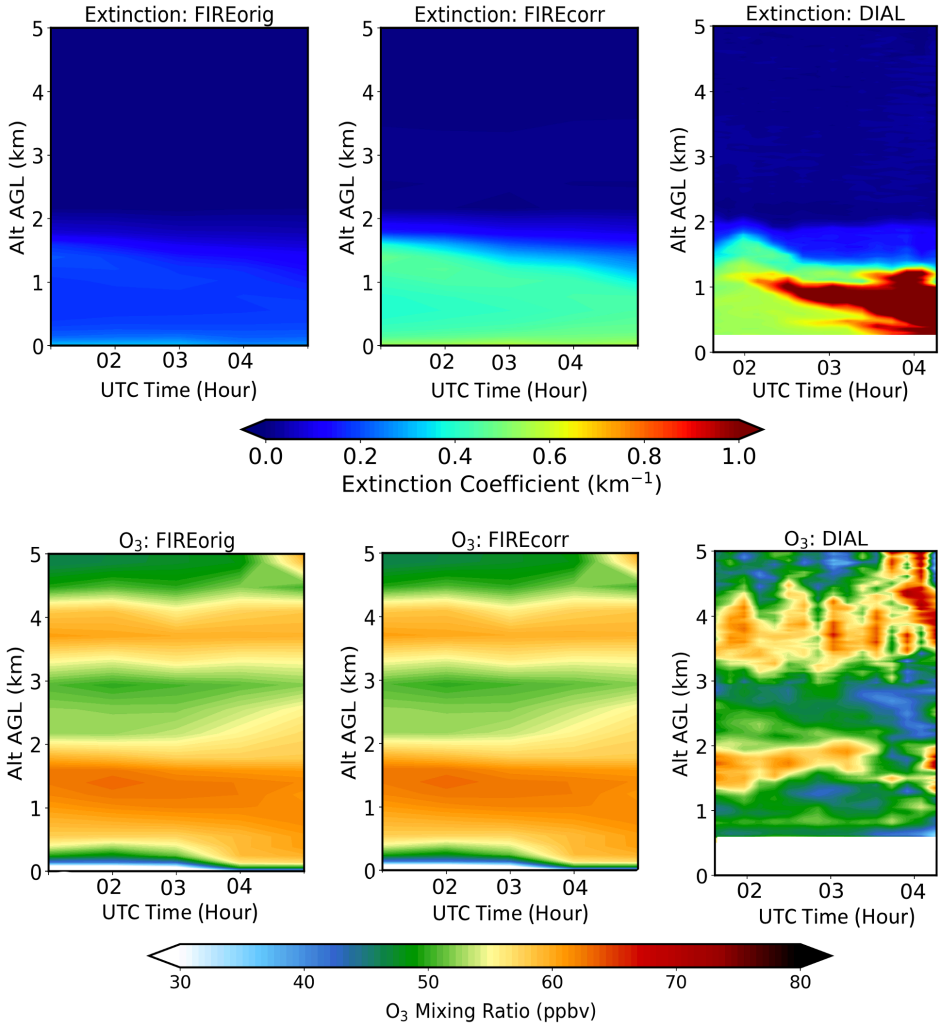

Figure 7. Modeled time-height curtain of aerosol extinction coefficient (at 300 nm) and ozone before (FIREorig) and after (FIREcorr) the emissions adjustment in 1–5 UTC on November 14 (19–23 LT on 13 November), compared with DIAL aerosol extinction (at 299 nm) and ozone.

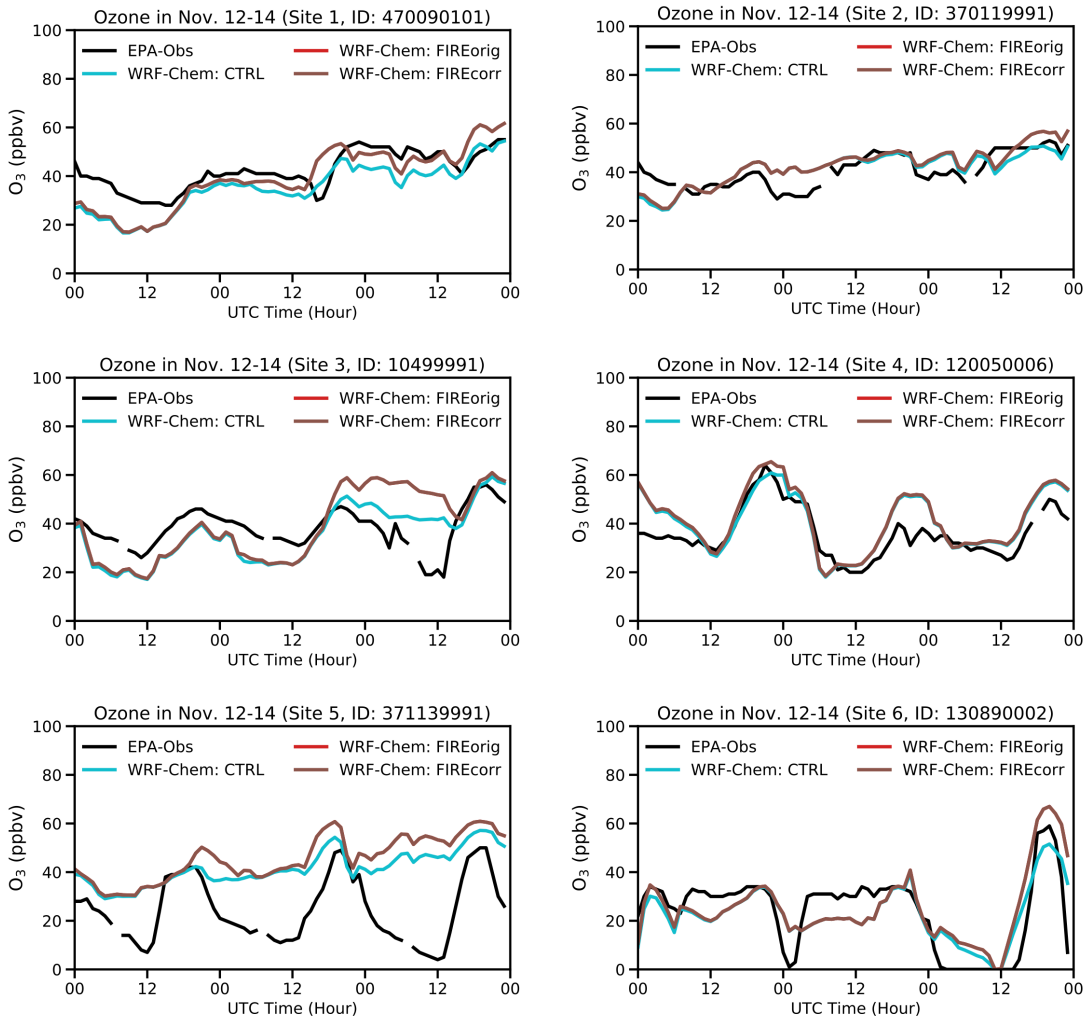

Figure 8. Comparison between EPA (black line) and WRF-Chem ozone in 12–14 November 2016 for control run (light blue), before correction (red), and after correction (brown). Pattern statistic can be seen in Figure S6. 6 EPA O_3 sites include: 1. Great Smoky Mountains NP-Look Rock, TN, 2. Cranberry, NC, 3. Sand Mountain, AL, 4. St.Andrews State Park, Panama City Beach, FL, 5. Coweeta, NC, 6. South DeKalb, GA.

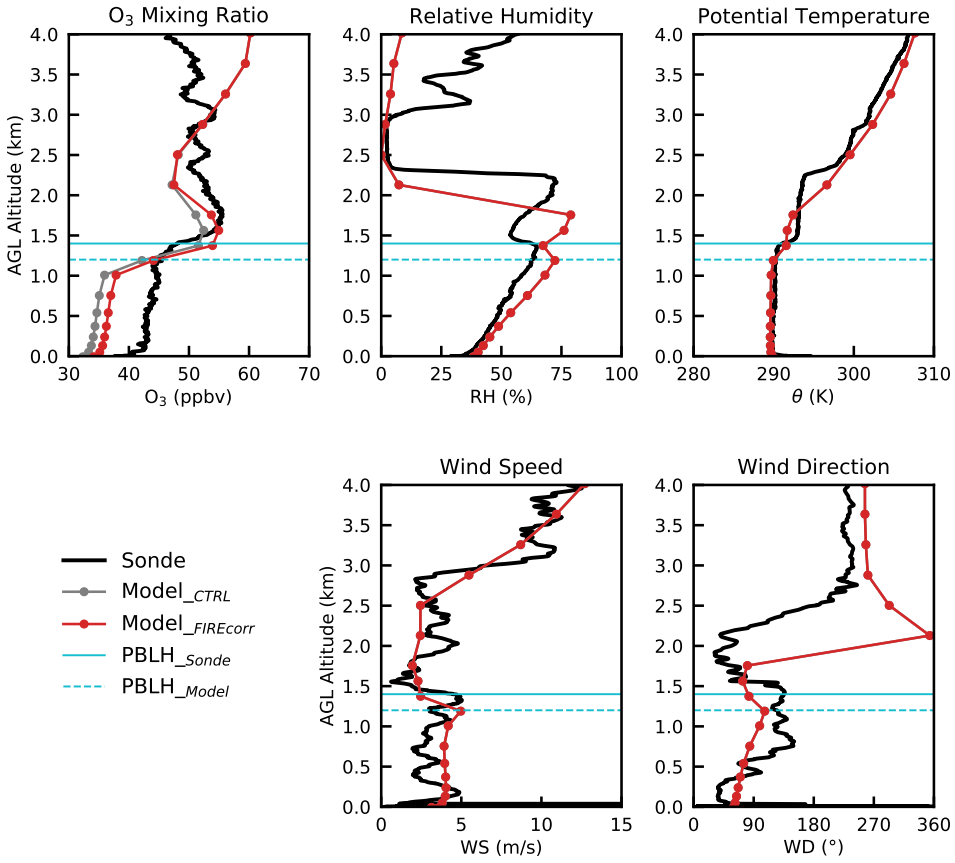

Figure 9. Comparison between ozonesonde (black color) and WRF-Chem simulations (FIREcorr in red color, CTRL in gray color) at 19 UTC (13 LT) on 12 November 2016. Ozone volume mixing ratio (O_3), relative humidity (RH), potential temperature (θ), horizontal wind speed (WS), and horizontal wind direction (WD) are displayed respectively. The aqua lines represent the PBL heights from sonde (solid line) and model (dashed line). Meteorological profiles and PBL height between FIREcorr and CTRL simulations are identical because the aerosol-radiation feedback is turned off.

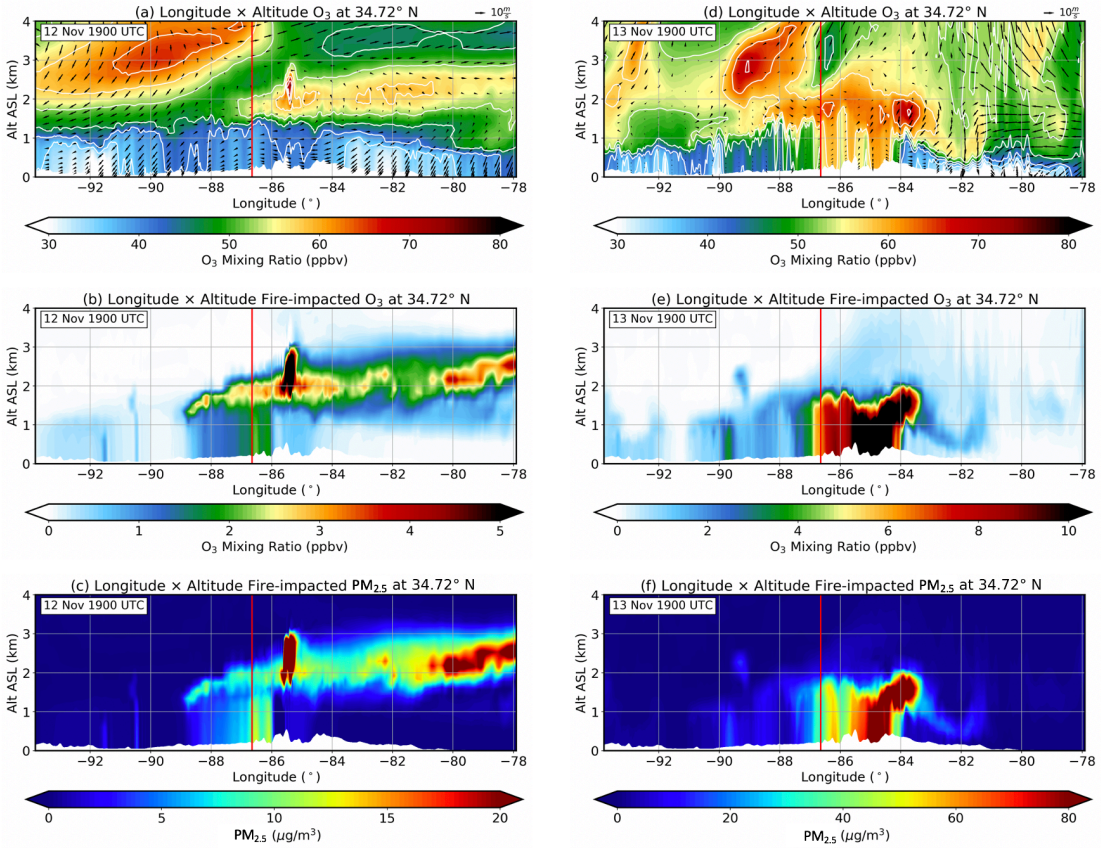

Figure 10. (a) Modeled (FIREcorr) vertical sections of O_3 mixing ratio (ppb) along an east-west transect (the magenta line shown in Figure 1) across Huntsville latitude (34.72° N) at 19 UTC (13 LT) on 12 November 2016 at 0–4 km ASL altitude. Solid red line denotes the longitude of Huntsville. Arrows indicate modeled direction and speed of horizontal wind. (b) Same as Figure a, but for fire-impacted (FIREcorr minus CTRL) O_3 mixing ratio. Note the colorbar range is different from Figure a. (c) Same as Figure b, but for fire-impacted $PM_{2.5}$ concentration ($\mu g/m^3$). (d–f) Same as Figure a–c, respectively, but for 19 UTC (13 LT) on 13 November 2016.

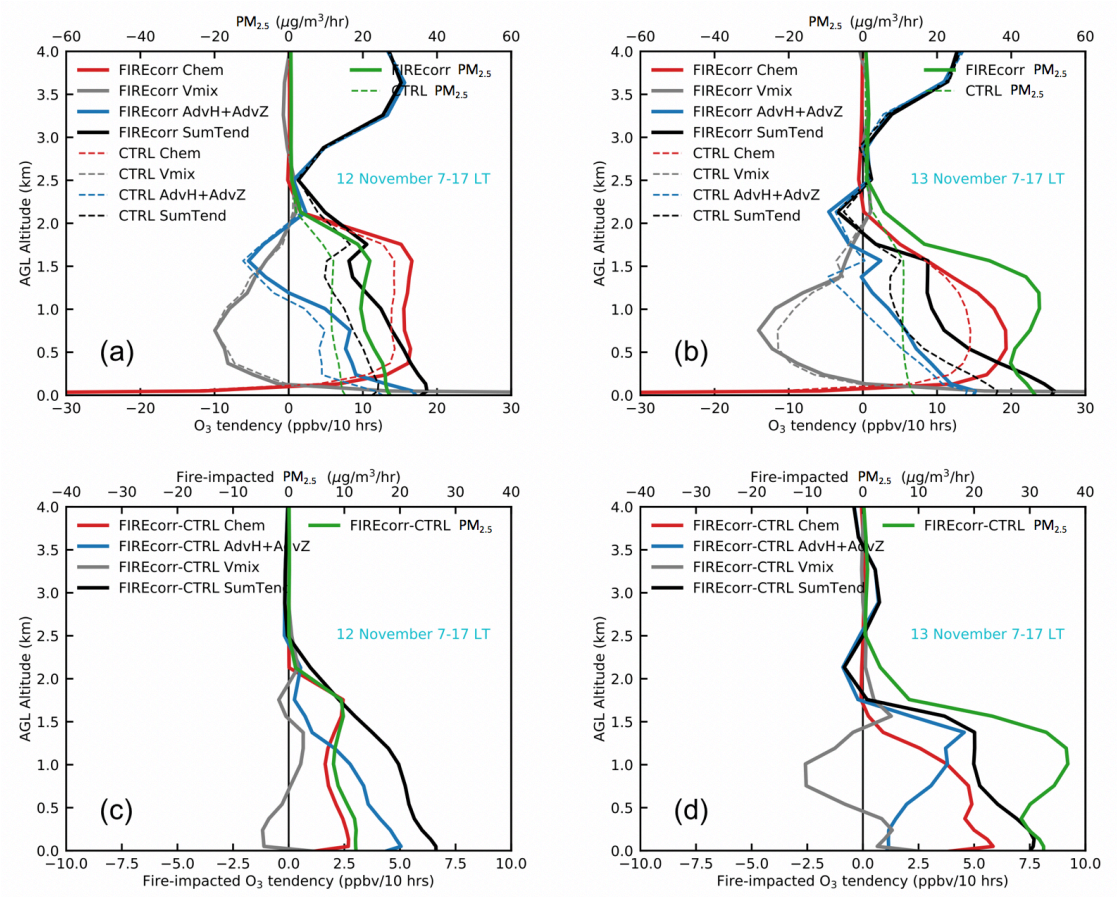

Figure 11. (a) and (b) Process analysis of daytime-integrated vertical ozone tendencies and daytime-averaged $PM_{2.5}$ over Huntsville in simulations with (FIREcorr, solid lines) and without (CTRL, dashed lines) fire emissions during 7–17 LT on 12 and 13 November, respectively. Processes include chemical reactions (Chem, red), horizontal and vertical advections (AdvH+AdvZ, blue), vertical mixing (Vmix, gray), and summed tendencies of all processes (SumTend, black). $PM_{2.5}$ is represented by green lines. (c) and (d) are same as Figure (a) and (b) but for fire-impacted values, calculated by the difference between FIREcorr and CTRL simulations.

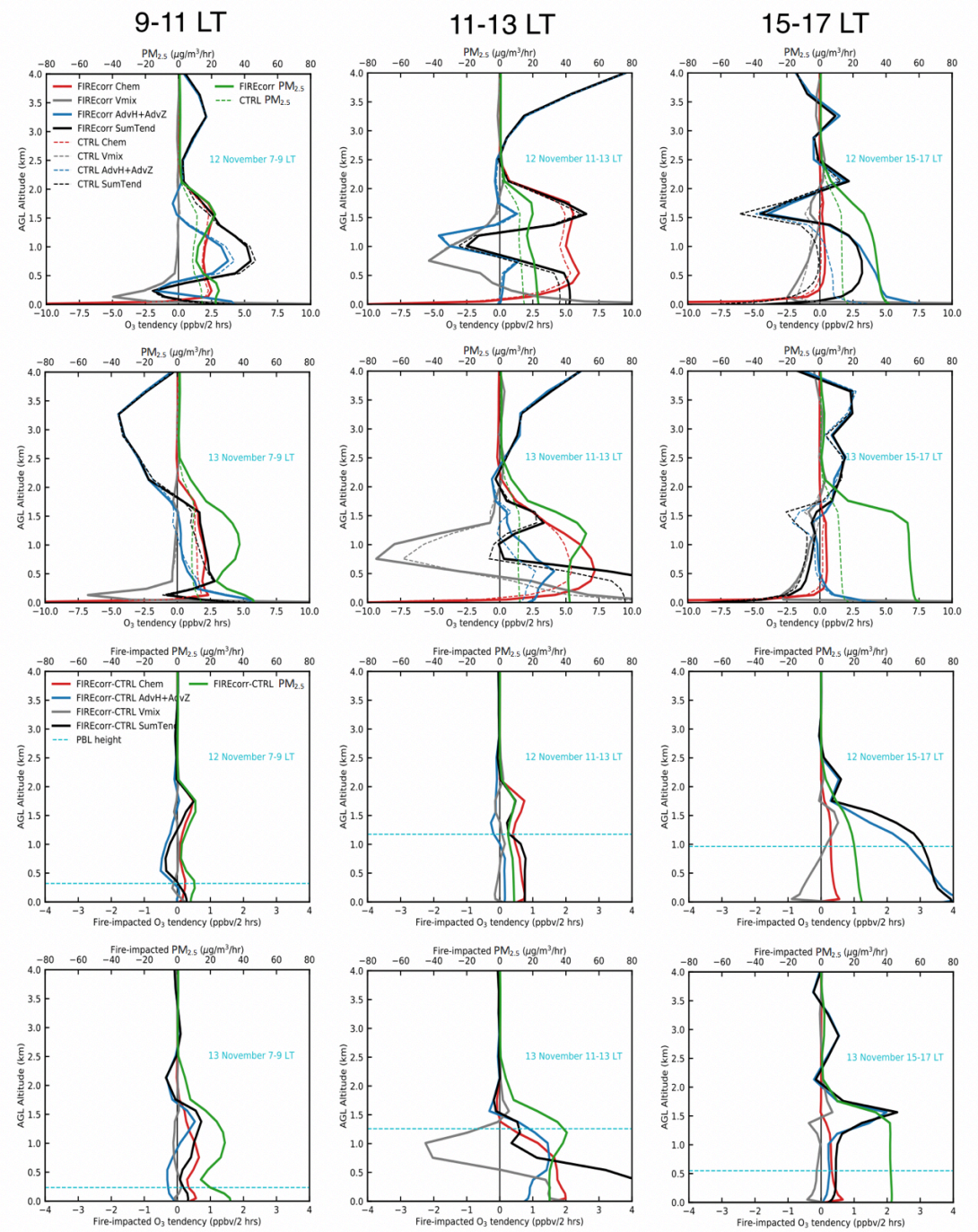

Figure 12. Same as **Figure 11**, but present diurnal variability by integrating 2 hours in 7–9, 11–13, and 15–17 LT on 12 November (row 1, 3) and 13 November (row 2, 4), respectively.

r2_study_area.

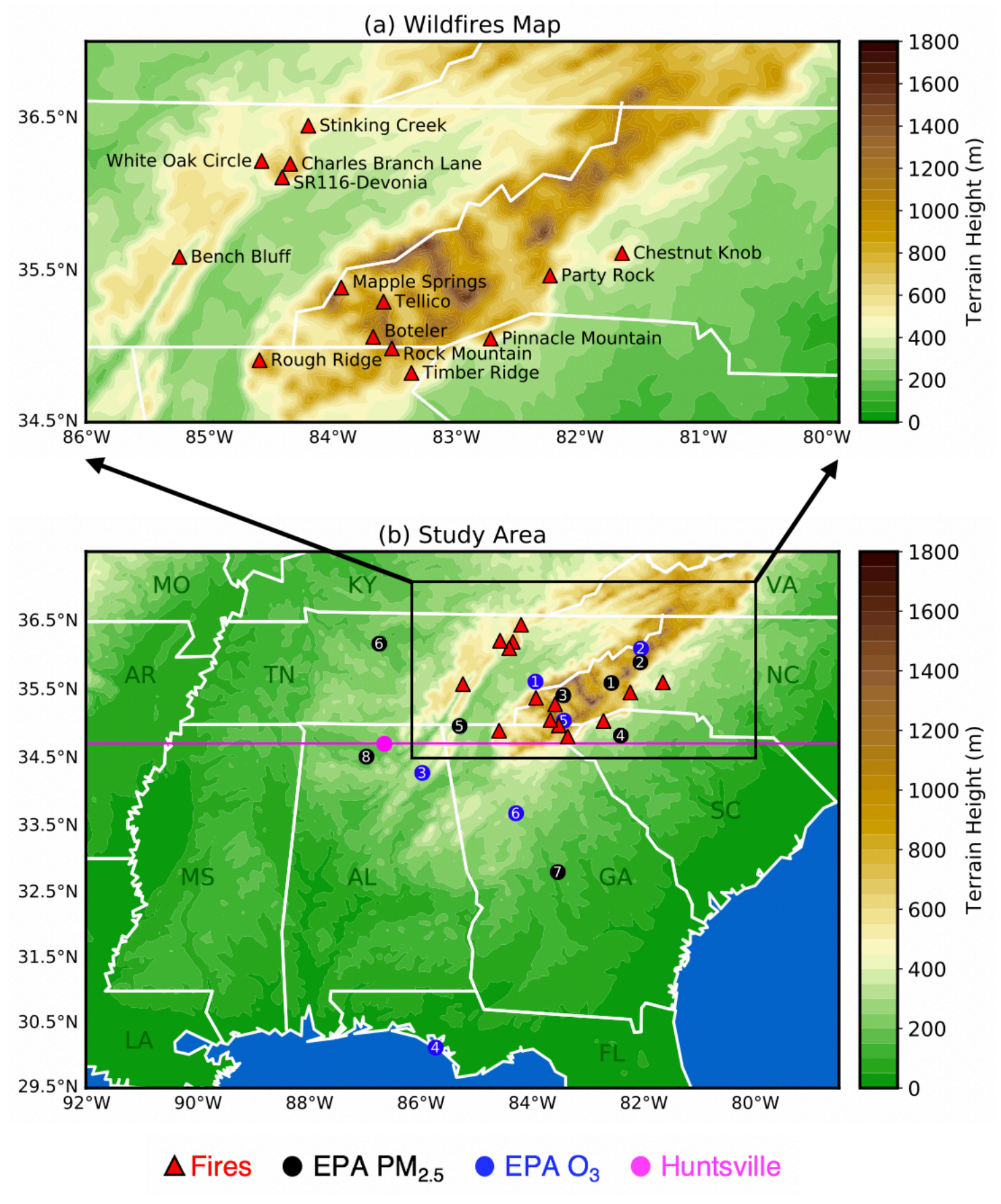
(a) Wildfires Map
Stinking Creek
White Oak Circle
Charles Branch Lane
SR116-Devonia
Bench Bluff
Chestnut Knob
Party Rock
Mapple Springs
Tellico
Boteler
Pinnacle Mountain
Rock Mountain
Rough Ridge
Timber Ridge
36.5°N
35.5°N
34.5°N
86°W
85°W
84°W
83°W
82°W
81°W
80°W
Terrain Height (m)
1800
1600
1400
1200
1000
800
600
400
200
0
(b) Study Area
MO
KY
VA
AR
TN
NC
SC
MS
AL
GA
LA
FL
36.5°N
35.5°N
34.5°N
33.5°N
32.5°N
31.5°N
30.5°N
29.5°N
92°W
90°W
88°W
86°W
84°W
82°W
80°W
Terrain Height (m)
1800
1600
1400
1200
1000
800
600
400
200
0
Fires
EPA PM2.5
EPA O3
Huntsville

burn_area.

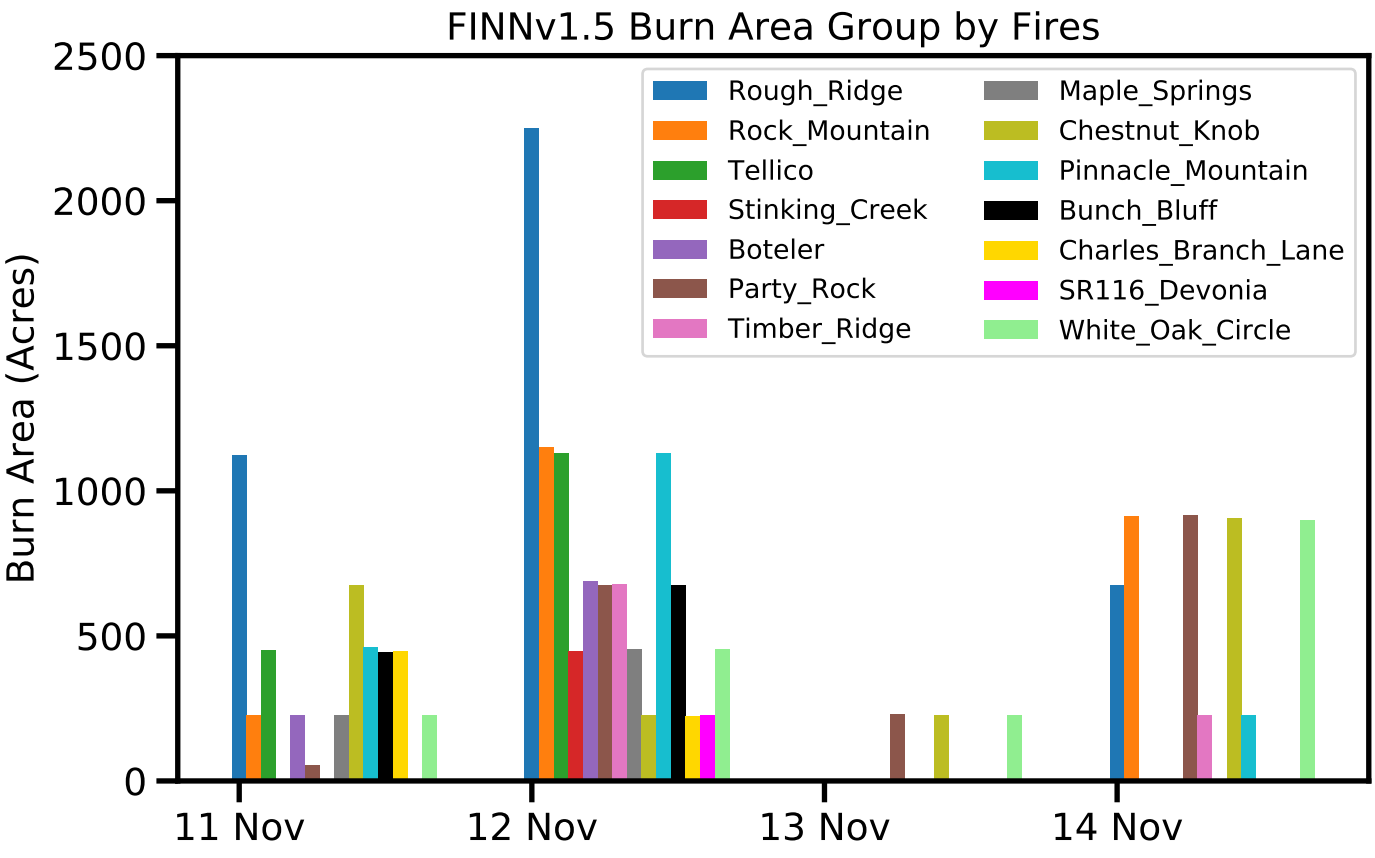
FINNv1.5 Burn Area Group by Fires
Burn Area (Acres)
2500
2000
1500
1000
500
0
11 Nov
12 Nov
13 Nov
14 Nov
Rough_Ridge
Rock_Mountain
Tellico
Stinking_Creek
Boteler
Party_Rock
Timber_Ridge
Maple_Springs
Chestnut_Knob
Pinnacle_Mountain
Bunch_Bluff
Charles_Branch_Lane
SR116_Devonia
White_Oak_Circle

r1_modis_model_AOD.

MODIS (Aqua and Terra) AOD

FIREorig Modeled AOD

FIREcorr Modeled AOD

MODIS Terra Corrected Reflectance

ceilometer_dial_v4.

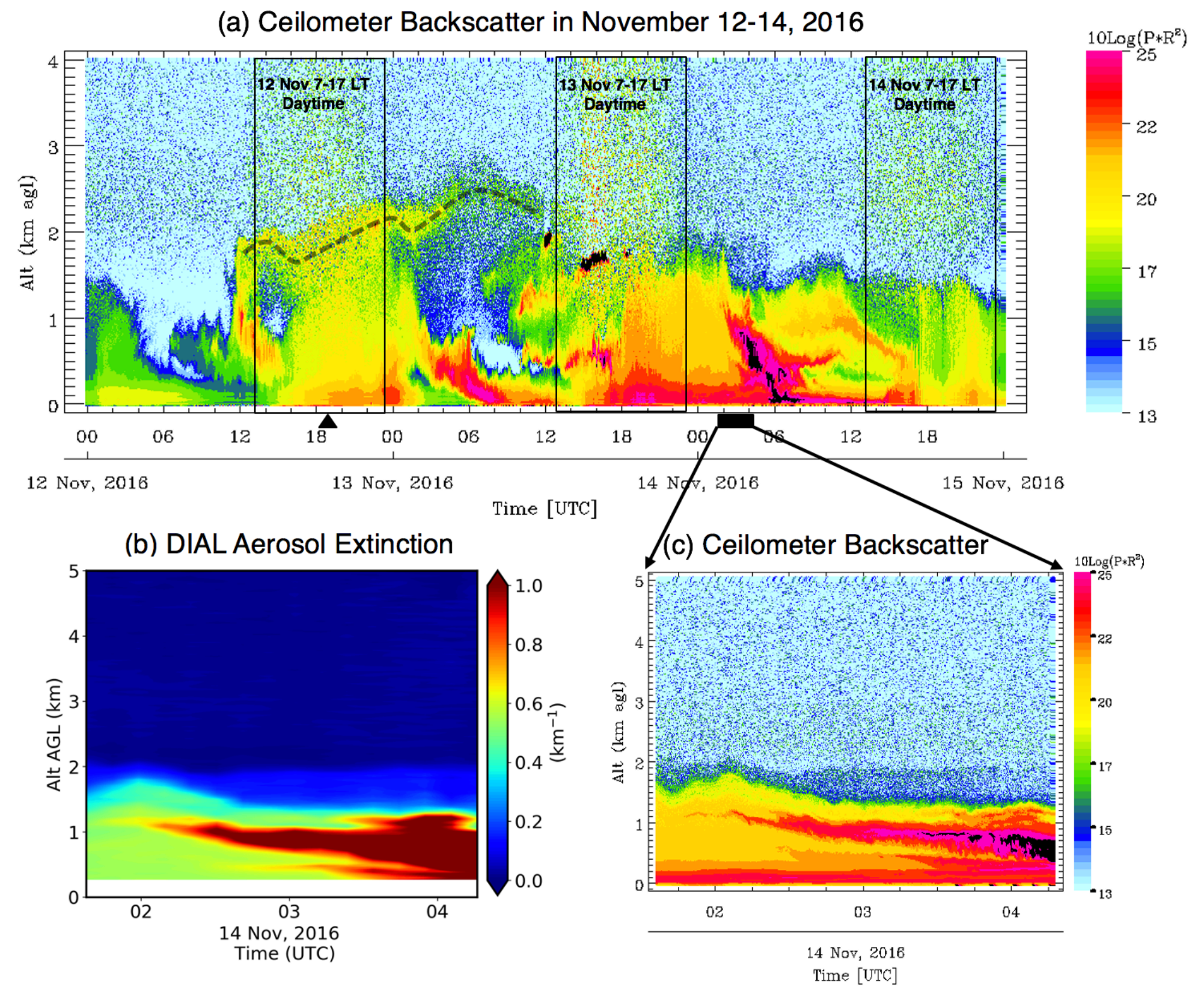
(a) Ceilometer Backscatter in November 12-14, 2016
12 Nov 7-17 LT Daytime
13 Nov 7-17 LT Daytime
14 Nov 7-17 LT Daytime
Alt (km agl)
10Log(P*R²)
12 Nov, 2016
13 Nov, 2016
14 Nov, 2016
15 Nov, 2016
Time [UTC]
(b) DIAL Aerosol Extinction
Alt AGL (km)
(km⁻¹)
14 Nov, 2016
Time (UTC)
(c) Ceilometer Backscatter
Alt (km agl)
14 Nov, 2016
Time [UTC]

r1_OCplusBCvsCO_Gg.

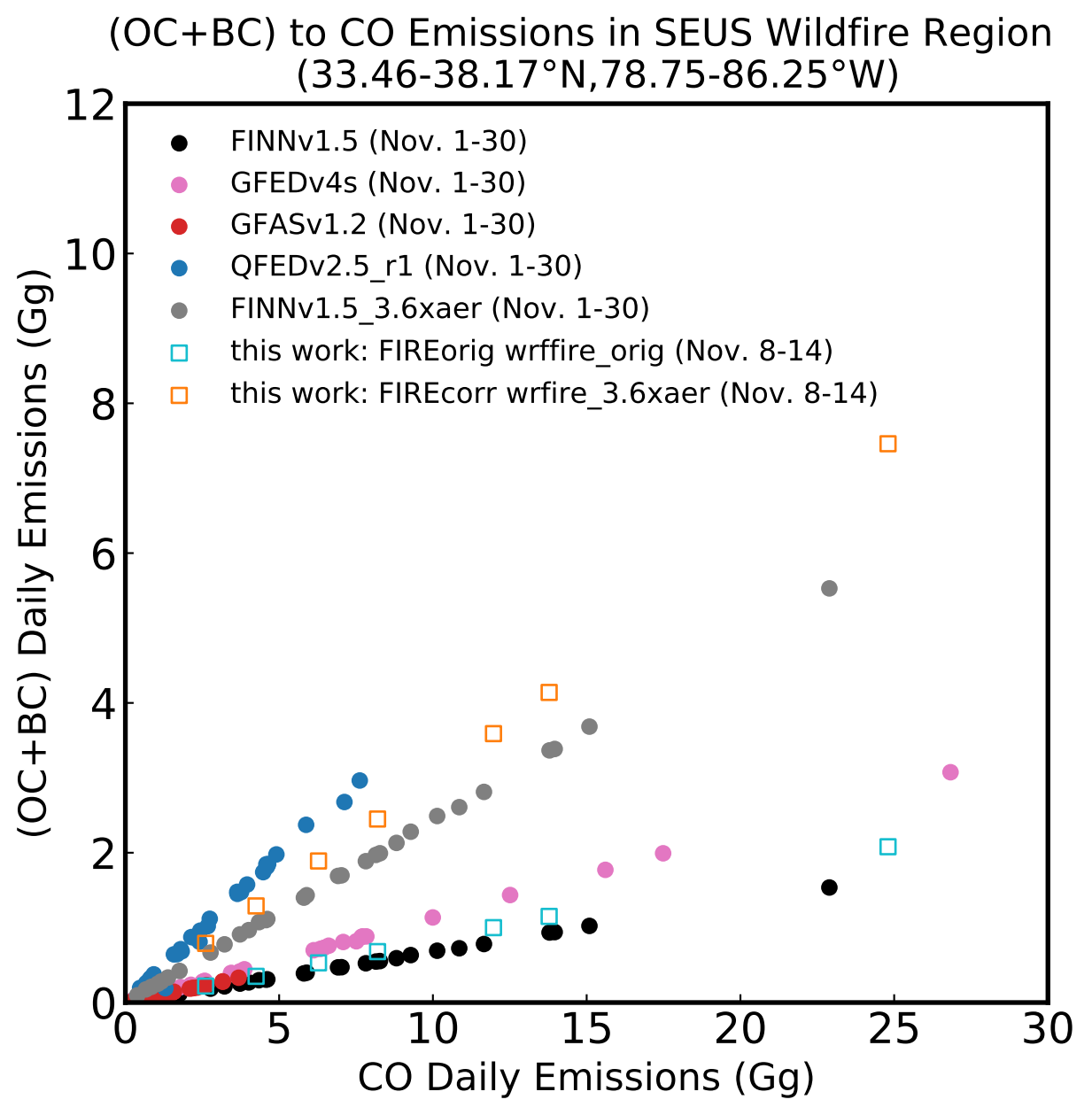
(OC+BC) to CO Emissions in SEUS Wildfire Region
(33.46-38.17°N,78.75-86.25°W)
FINNv1.5 (Nov. 1-30)
GFEDv4s (Nov. 1-30)
GFASv1.2 (Nov. 1-30)
QFEDv2.5_r1 (Nov. 1-30)
FINNv1.5_3.6xaer (Nov. 1-30)
this work: FIREorig wrffire_orig (Nov. 8-14)
this work: FIREcorr wrfire_3.6xaer (Nov. 8-14)
(OC+BC) Daily Emissions (Gg)
CO Daily Emissions (Gg)
0
2
4
6
8
10
12
0
5
10
15
20
25
30

r2_wrfchem_pm25.

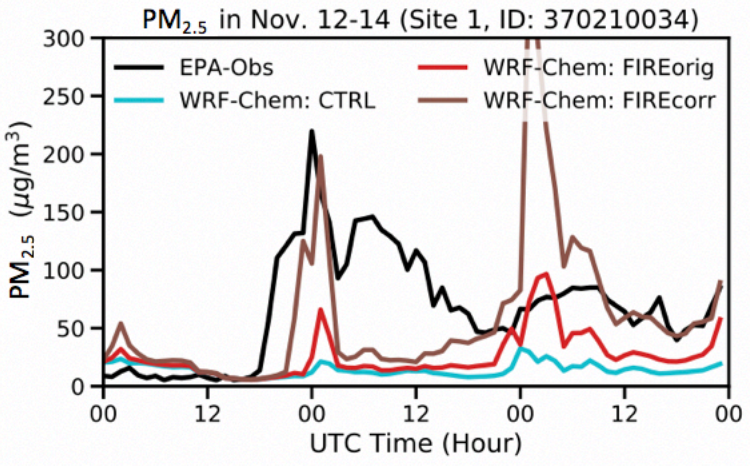
PM2.5 in Nov. 12-14 (Site 1, ID: 370210034)
EPA-Obs
WRF-Chem: CTRL
WRF-Chem: FIREorig
WRF-Chem: FIREcorr
PM2.5 (μg/m3)
UTC Time (Hour)

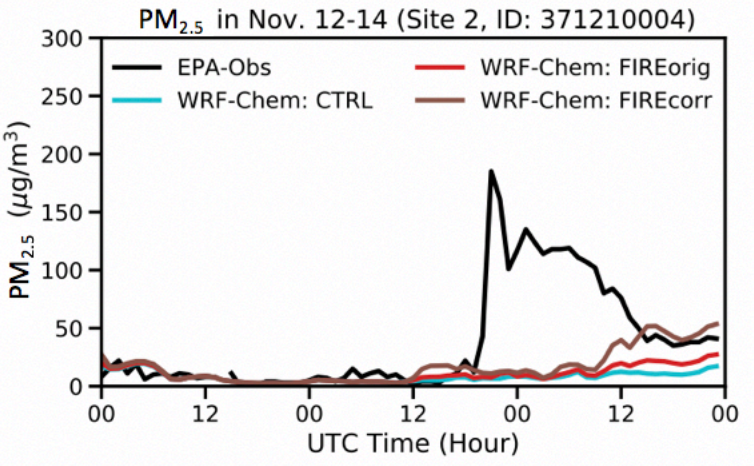
PM2.5 in Nov. 12-14 (Site 2, ID: 371210004)
EPA-Obs
WRF-Chem: CTRL
WRF-Chem: FIREorig
WRF-Chem: FIREcorr
PM2.5 (μg/m3)
UTC Time (Hour)

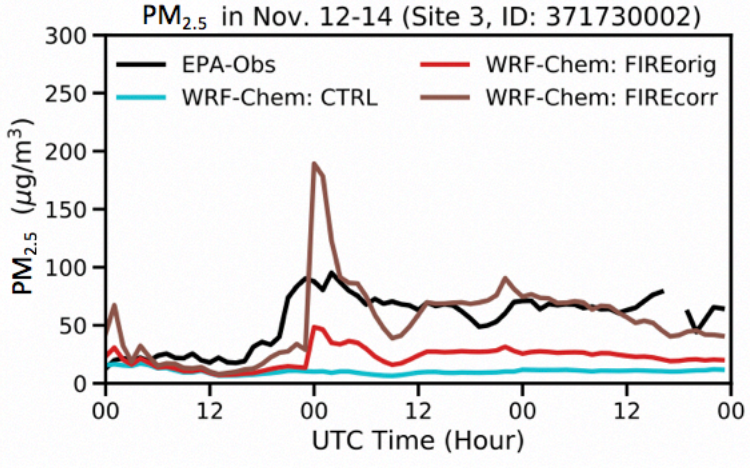
PM2.5 in Nov. 12-14 (Site 3, ID: 371730002)
EPA-Obs
WRF-Chem: CTRL
WRF-Chem: FIREorig
WRF-Chem: FIREcorr
PM2.5 (μg/m3)
UTC Time (Hour)

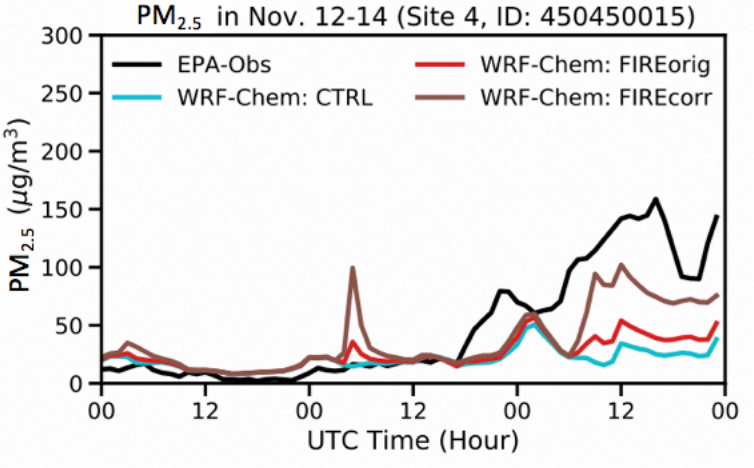
PM2.5 in Nov. 12-14 (Site 4, ID: 450450015)
EPA-Obs
WRF-Chem: CTRL
WRF-Chem: FIREorig
WRF-Chem: FIREcorr
PM2.5 (μg/m3)
UTC Time (Hour)

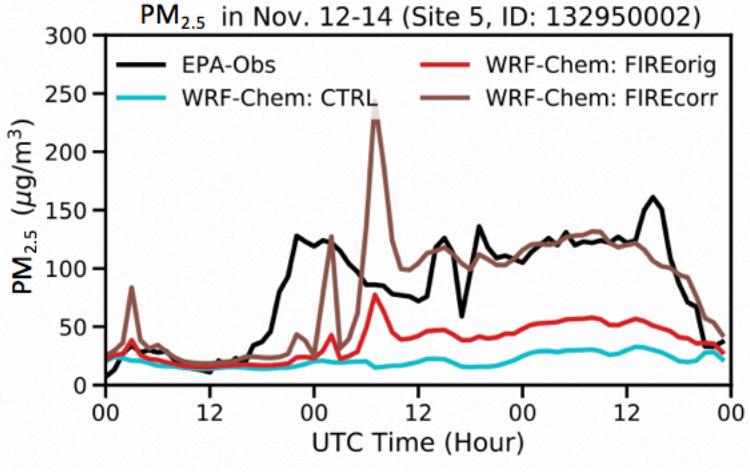
PM2.5 in Nov. 12-14 (Site 5, ID: 132950002)
EPA-Obs
WRF-Chem: CTRL
WRF-Chem: FIREorig
WRF-Chem: FIREcorr
PM2.5 (μg/m3)
UTC Time (Hour)

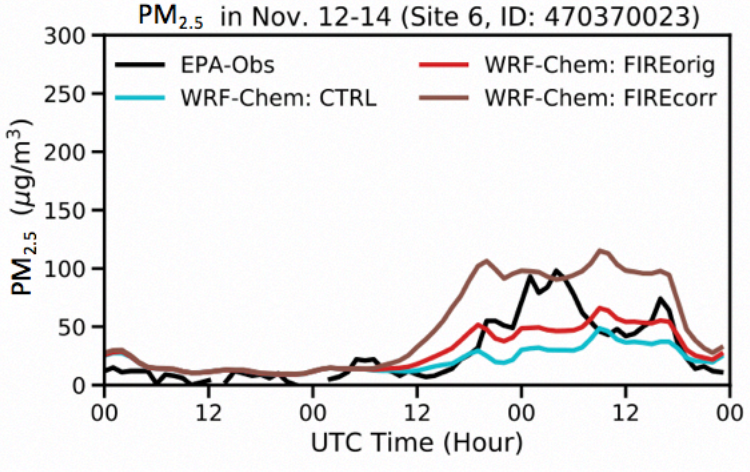
PM2.5 in Nov. 12-14 (Site 6, ID: 470370023)
EPA-Obs
WRF-Chem: CTRL
WRF-Chem: FIREorig
WRF-Chem: FIREcorr
PM2.5 (μg/m3)
UTC Time (Hour)

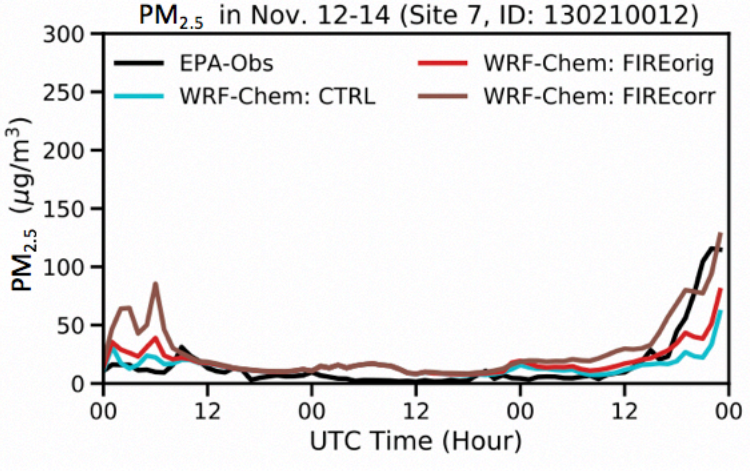
PM2.5 in Nov. 12-14 (Site 7, ID: 130210012)
EPA-Obs
WRF-Chem: CTRL
WRF-Chem: FIREorig
WRF-Chem: FIREcorr
PM2.5 (μg/m3)
UTC Time (Hour)

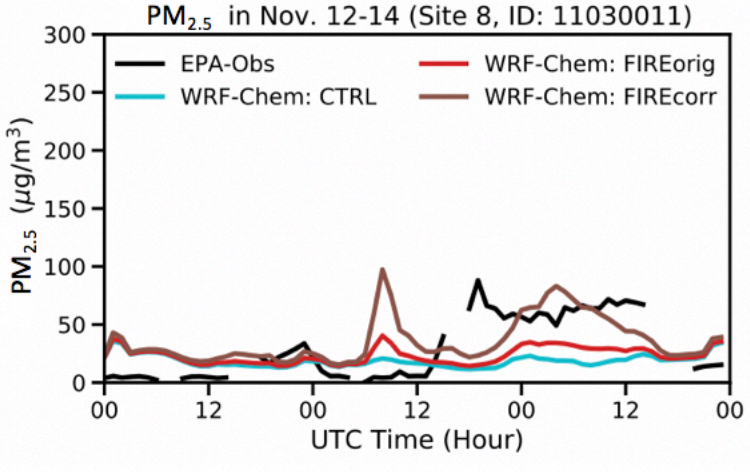
PM2.5 in Nov. 12-14 (Site 8, ID: 11030011)
EPA-Obs
WRF-Chem: CTRL
WRF-Chem: FIREorig
WRF-Chem: FIREcorr
PM2.5 (μg/m3)
UTC Time (Hour)

ext_o3_evaluation_v2.

Extinction: FIREorig

Extinction: FIREcorr

Extinction: DIAL

Alt AGL (km)

UTC Time (Hour)

0.0 0.2 0.4 0.6 0.8 1.0

Extinction Coefficient (km^{-1})

O_3: FIREorig

O_3: FIREcorr

O_3: DIAL

30 40 50 60 70 80

O_3 Mixing Ratio (ppbv)

wrfchem_ozone_v2.

Ozone in Nov. 12-14 (Site 1, ID: 470090101)

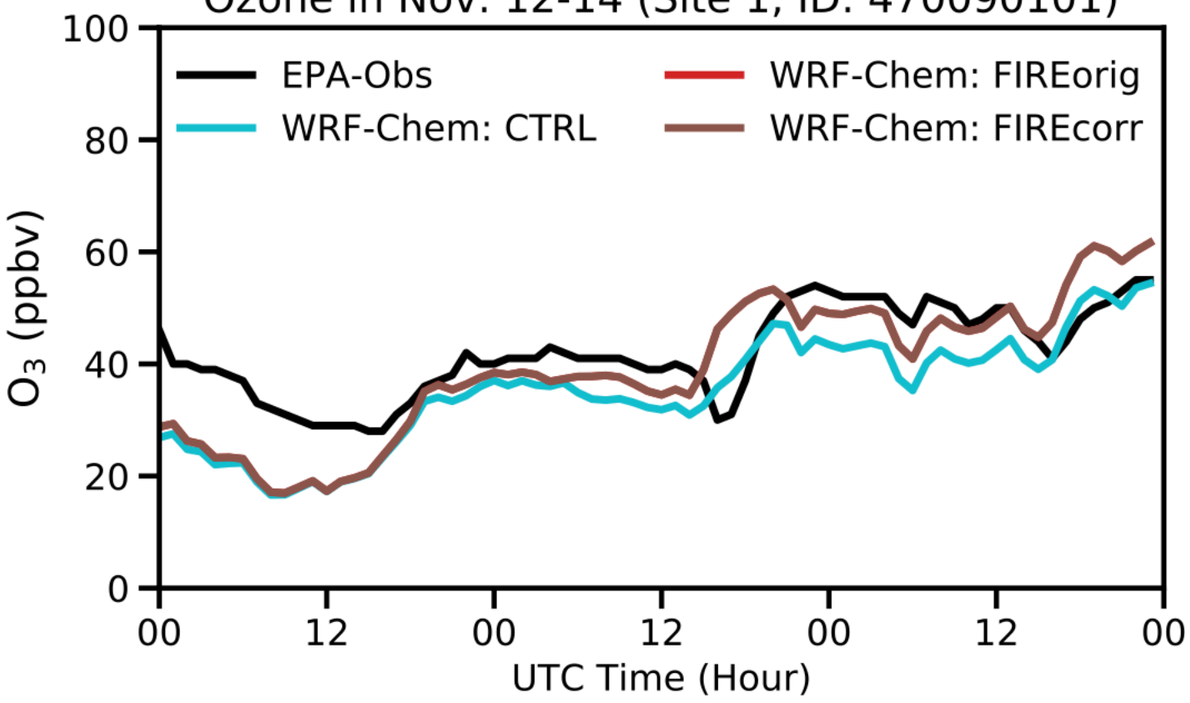

Ozone in Nov. 12-14 (Site 2, ID: 370119991)

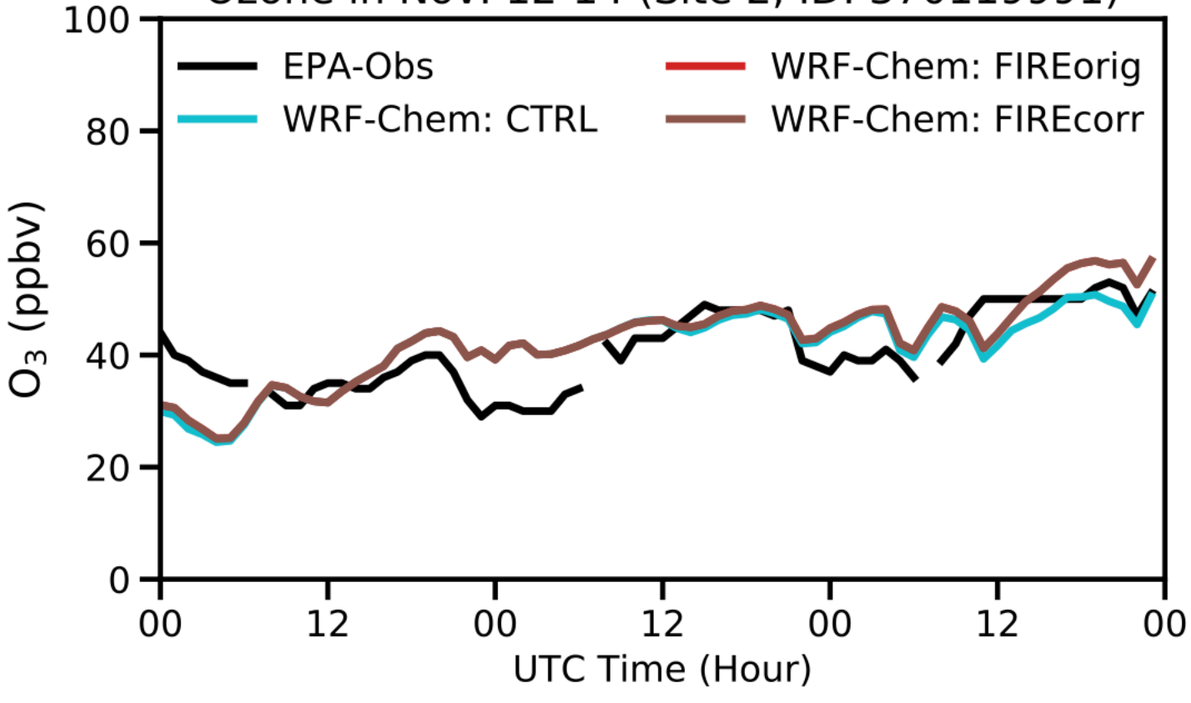

Ozone in Nov. 12-14 (Site 3, ID: 10499991)

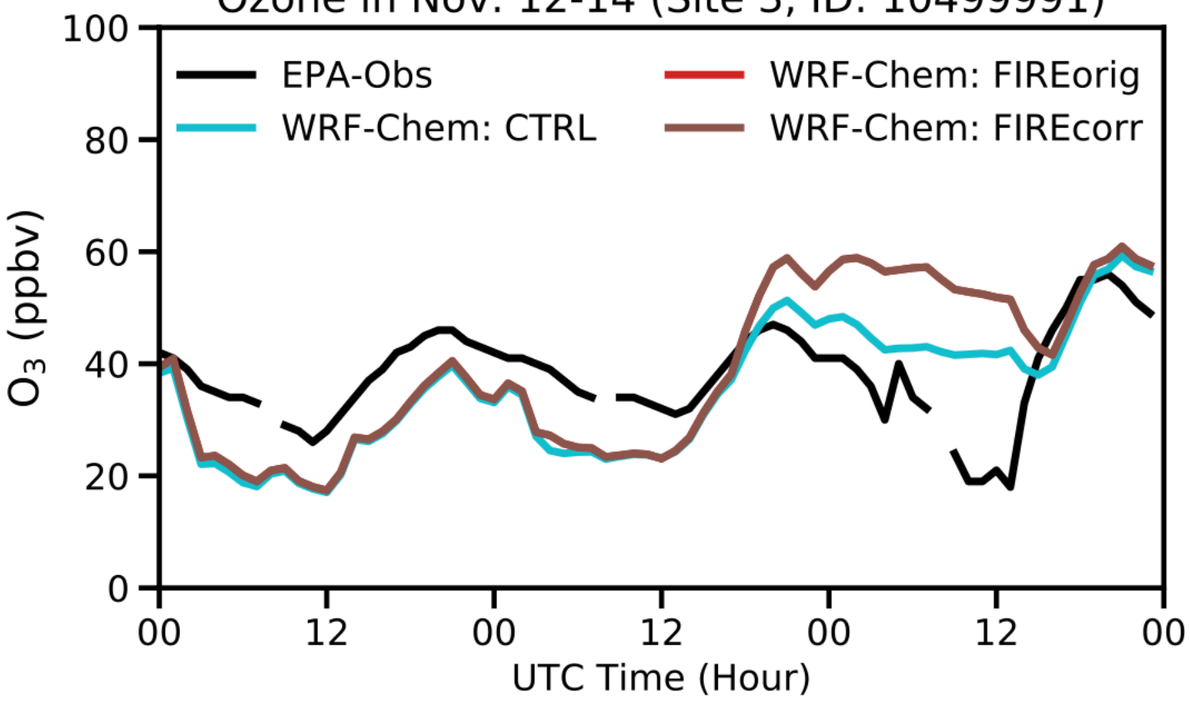

Ozone in Nov. 12-14 (Site 4, ID: 120050006)

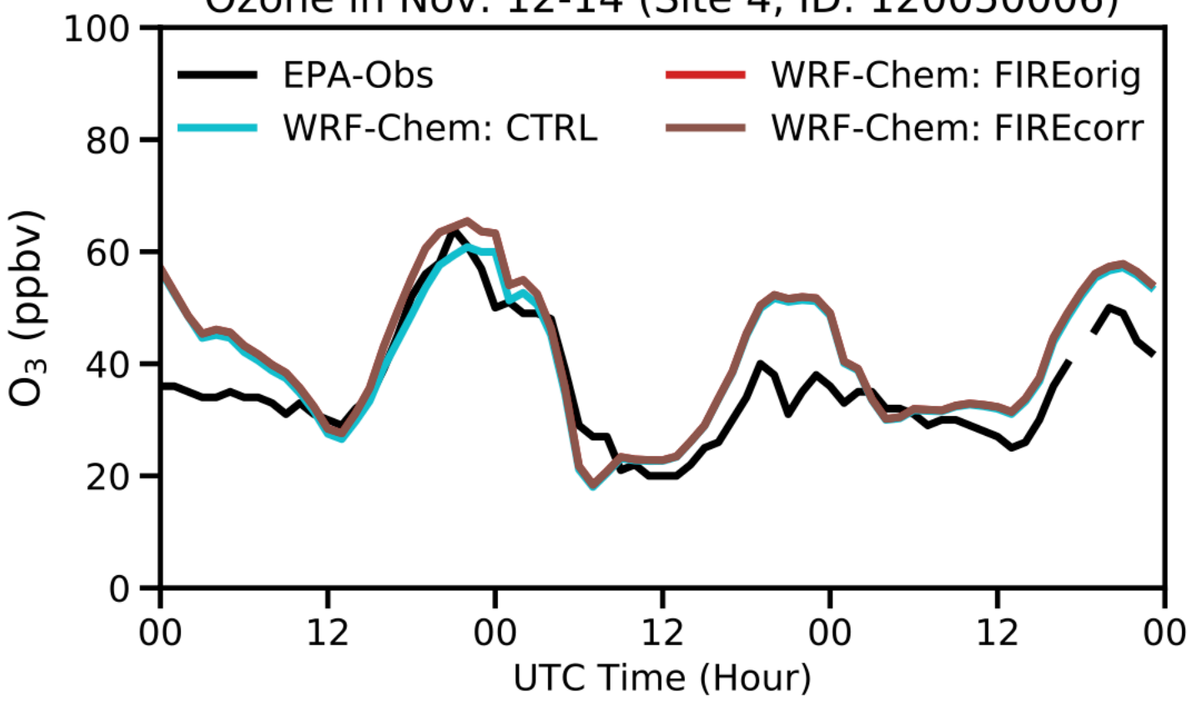

Ozone in Nov. 12-14 (Site 5, ID: 371139991)

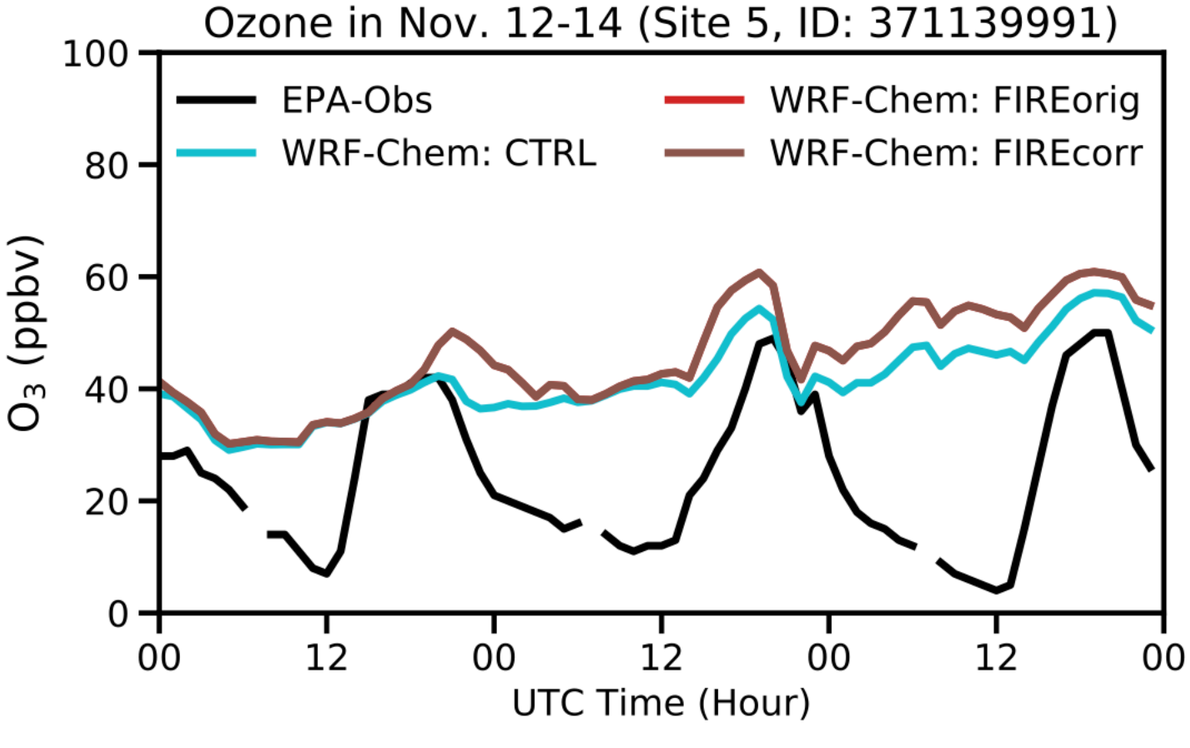

Ozone in Nov. 12-14 (Site 6, ID: 130890002)

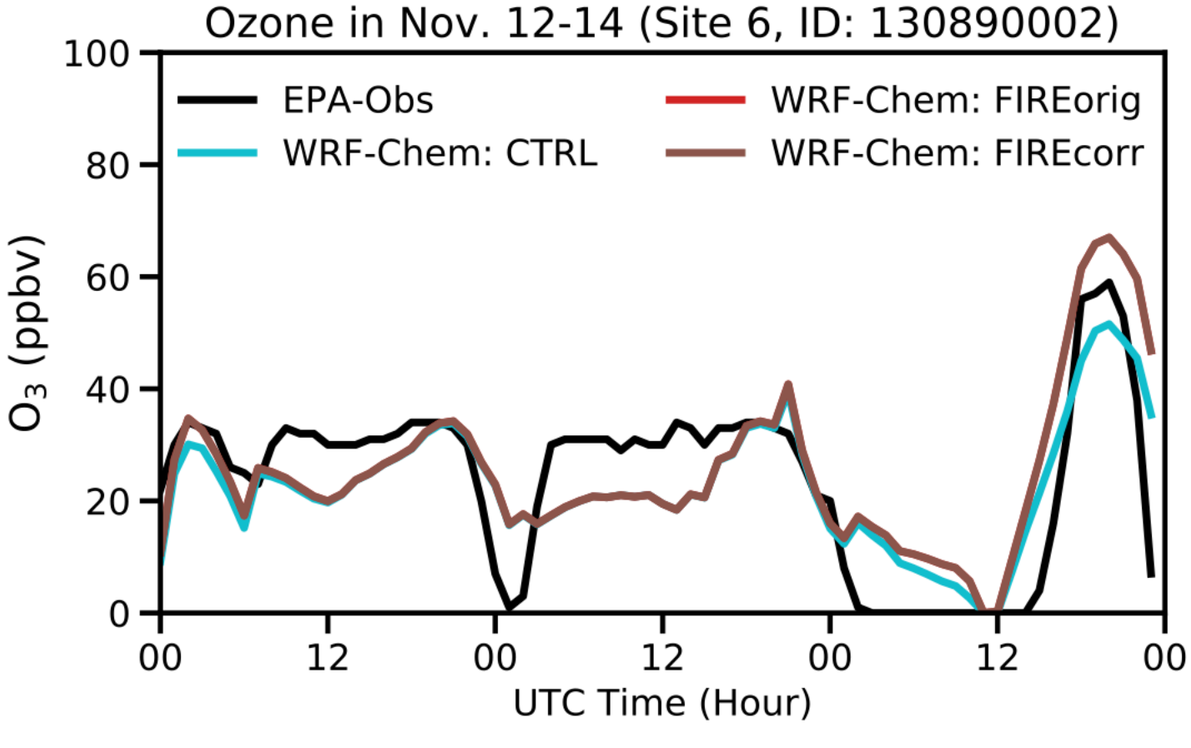

r1_HU995_20161112_wofb.

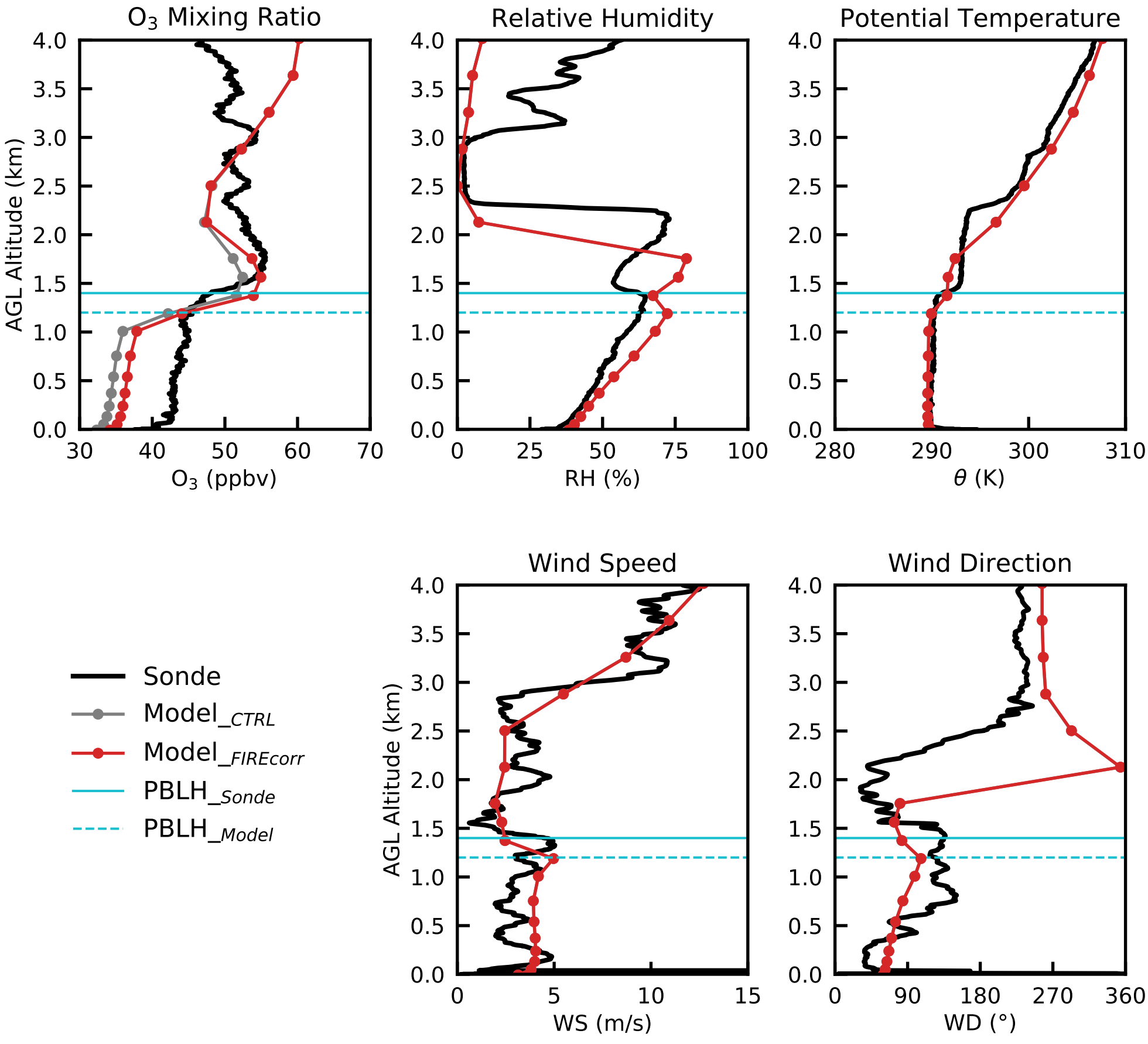
O3 Mixing Ratio
Relative Humidity
Potential Temperature
AGL Altitude (km)
O3 (ppbv)
RH (%)
θ (K)
Wind Speed
Wind Direction
WS (m/s)
WD (°)
Sonde
Model_CTRL
Model_FIREcorr
PBLH_Sonde
PBLH_Model

r2_alt_lon_nov12-13_wofb.

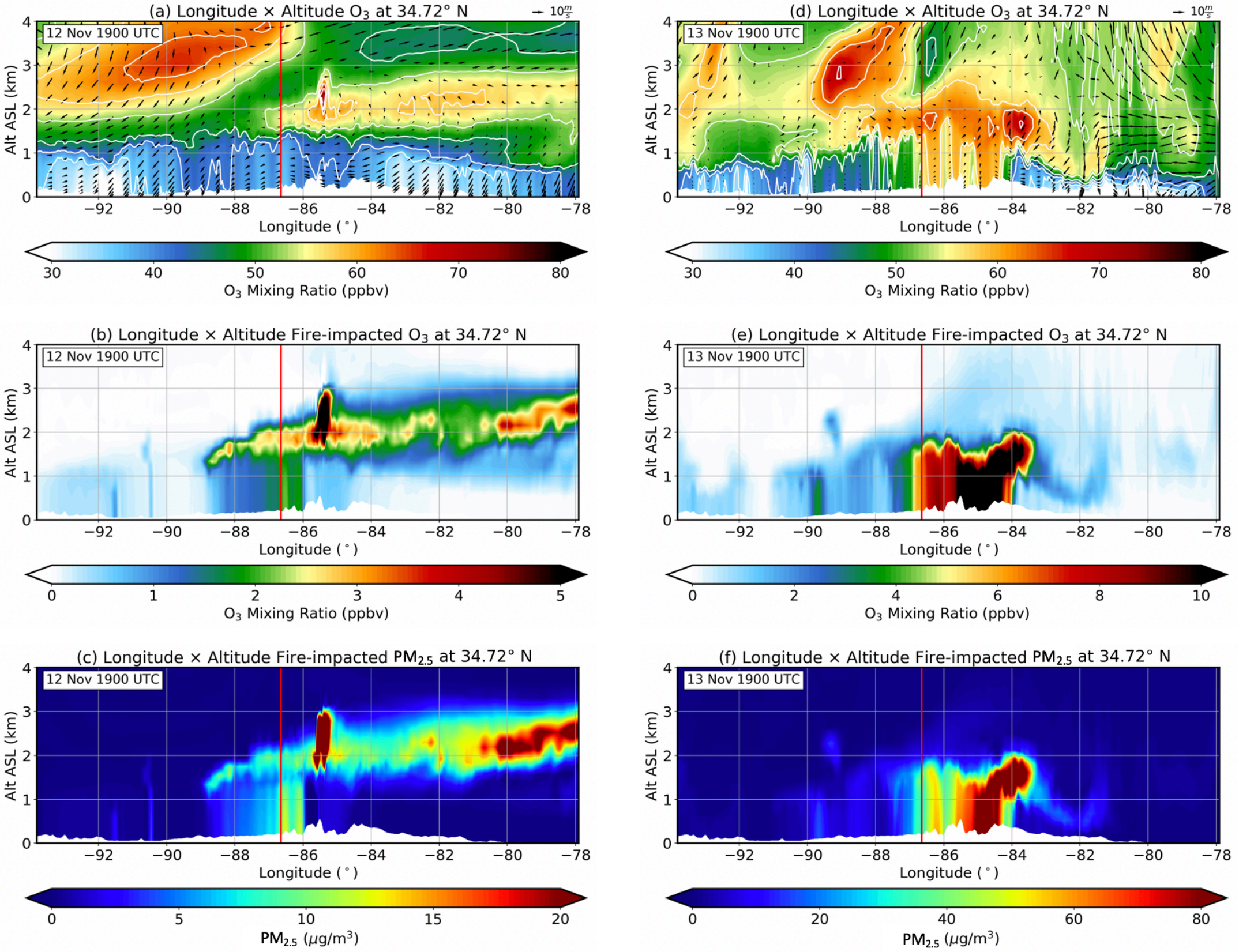
(a) Longitude × Altitude O_3 at 34.72° N
12 Nov 1900 UTC
Alt ASL (km)
Longitude (°)
O_3 Mixing Ratio (ppbv)
(d) Longitude × Altitude O_3 at 34.72° N
13 Nov 1900 UTC
(b) Longitude × Altitude Fire-impacted O_3 at 34.72° N
(e) Longitude × Altitude Fire-impacted O_3 at 34.72° N
(c) Longitude × Altitude Fire-impacted $PM_{2.5}$ at 34.72° N
$PM_{2.5}$ ($\mu g/m^3$)
(f) Longitude × Altitude Fire-impacted $PM_{2.5}$ at 34.72° N

r2_daytime_tendency.

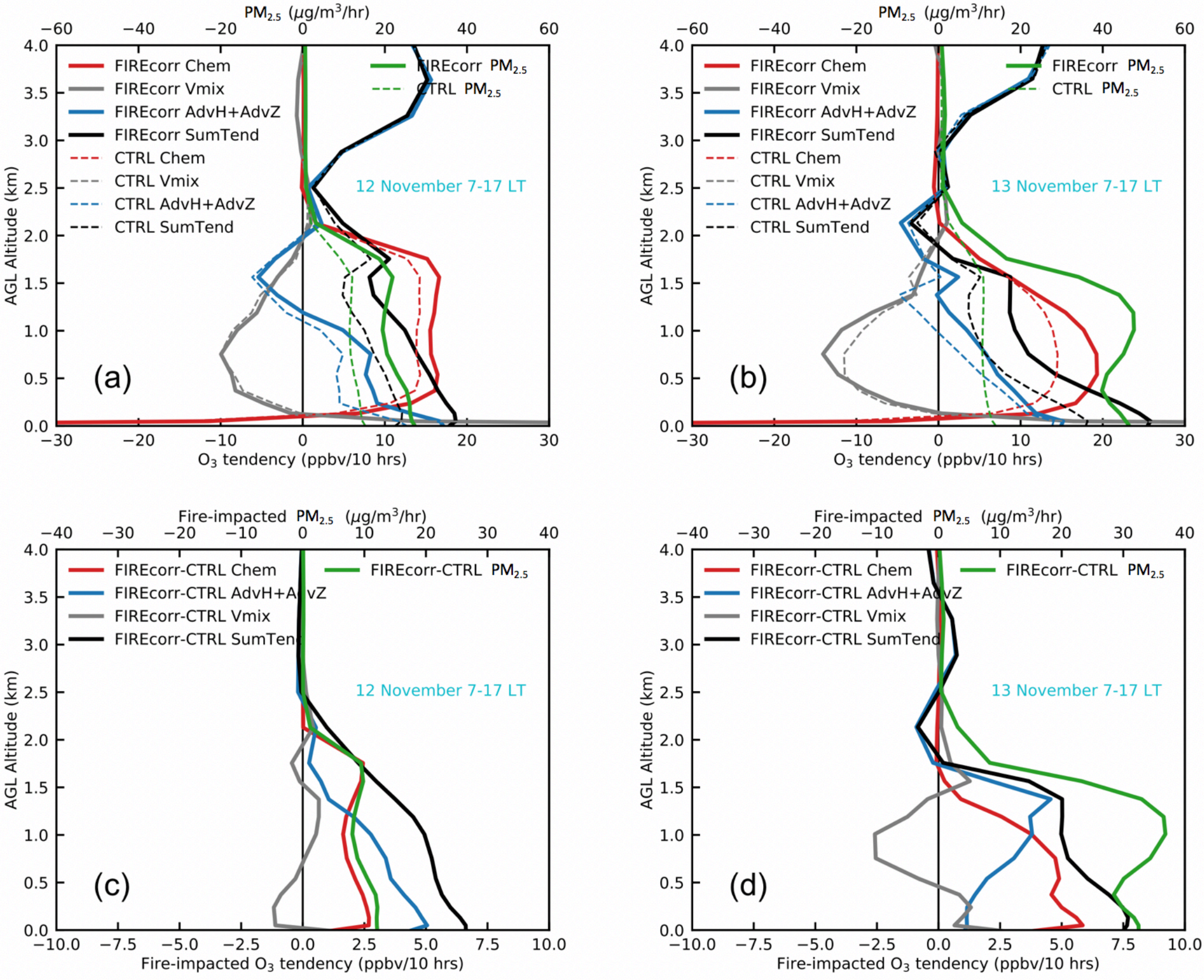
PM2.5 (μg/m3/hr)
FIREcorr Chem
FIREcorr Vmix
FIREcorr AdvH+AdvZ
FIREcorr SumTend
CTRL Chem
CTRL Vmix
CTRL AdvH+AdvZ
CTRL SumTend
FIREcorr PM2.5
CTRL PM2.5
12 November 7-17 LT
(a)
AGL Altitude (km)
O3 tendency (ppbv/10 hrs)
PM2.5 (μg/m3/hr)
13 November 7-17 LT
(b)
Fire-impacted PM2.5 (μg/m3/hr)
FIREcorr-CTRL Chem
FIREcorr-CTRL AdvH+AdvZ
FIREcorr-CTRL Vmix
FIREcorr-CTRL SumTend
FIREcorr-CTRL PM2.5
(c)
Fire-impacted O3 tendency (ppbv/10 hrs)
(d)

r2_2hr_tendency.

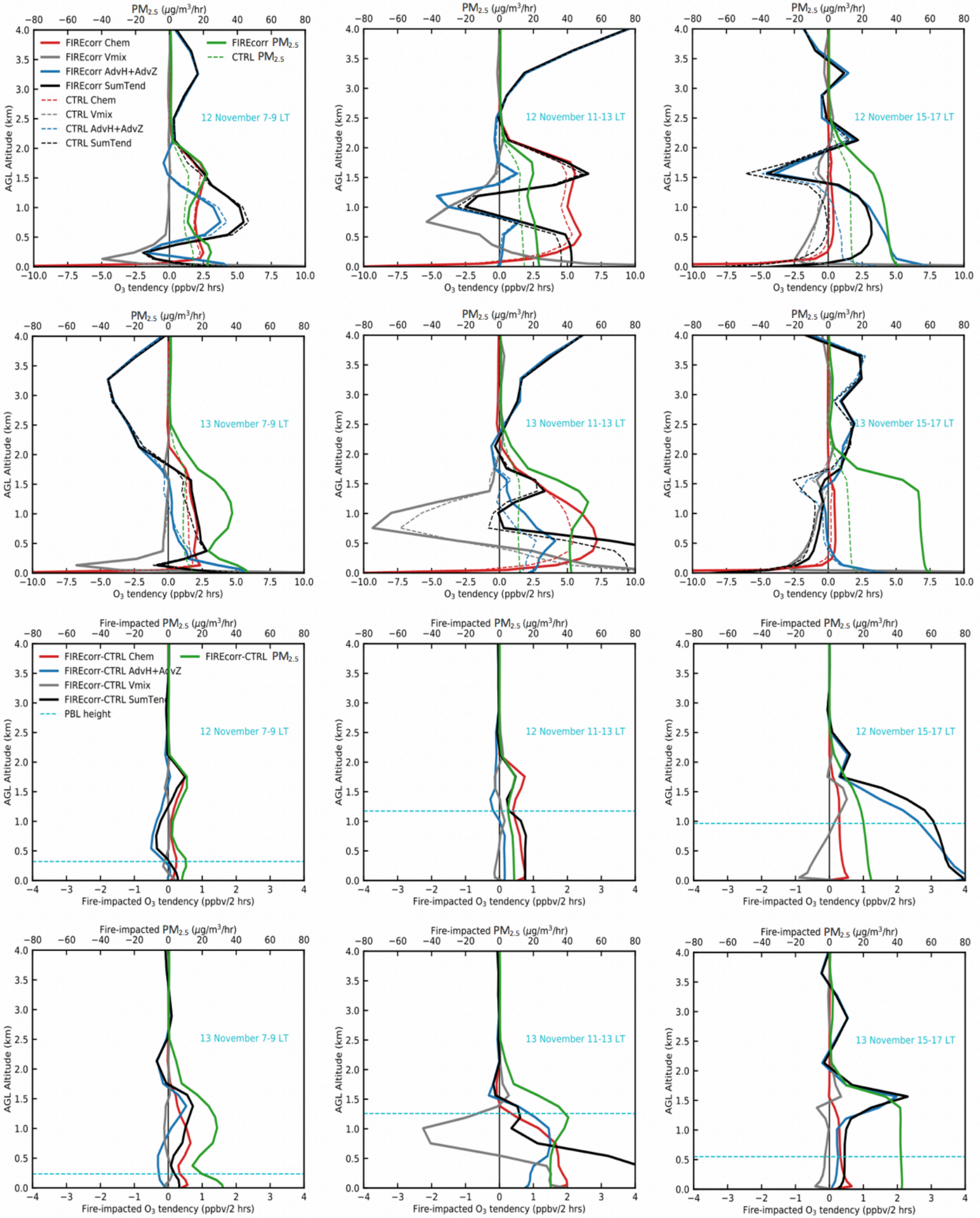
9-11 LT
11-13 LT
15-17 LT
PM2.5 (μg/m3/hr)
FIREcorr Chem
FIREcorr Vmix
FIREcorr AdvH+AdvZ
FIREcorr SumTend
CTRL Chem
CTRL Vmix
CTRL AdvH+AdvZ
CTRL SumTend
FIREcorr PM2.5
CTRL PM2.5
12 November 7-9 LT
12 November 11-13 LT
12 November 15-17 LT
13 November 7-9 LT
13 November 11-13 LT
13 November 15-17 LT
AGL Altitude (km)
O3 tendency (ppbv/2 hrs)
Fire-impacted PM2.5 (μg/m3/hr)
FIREcorr-CTRL Chem
FIREcorr-CTRL AdvH+AdvZ
FIREcorr-CTRL Vmix
FIREcorr-CTRL SumTend
FIREcorr-CTRL PM2.5
PBL height
Fire-impacted O3 tendency (ppbv/2 hrs)